Oncogenic signals prime cancer cells for toxic cell overgrowth during a G1 cell cycle arrest

Foy, Reece; Crozier, Lisa; Pareri, Aanchal U.; Valverde, Juan Manuel; Ho Park, Ben; Ly, Tony

Published in:
Molecular Cell

DOI:
10.1016/j.molcel.2023.10.020

Publication date:
2023

Molecular Cell

Article

Oncogenic signals prime cancer cells for toxic cell overgrowth during a G1 cell cycle arrest

Graphical abstract

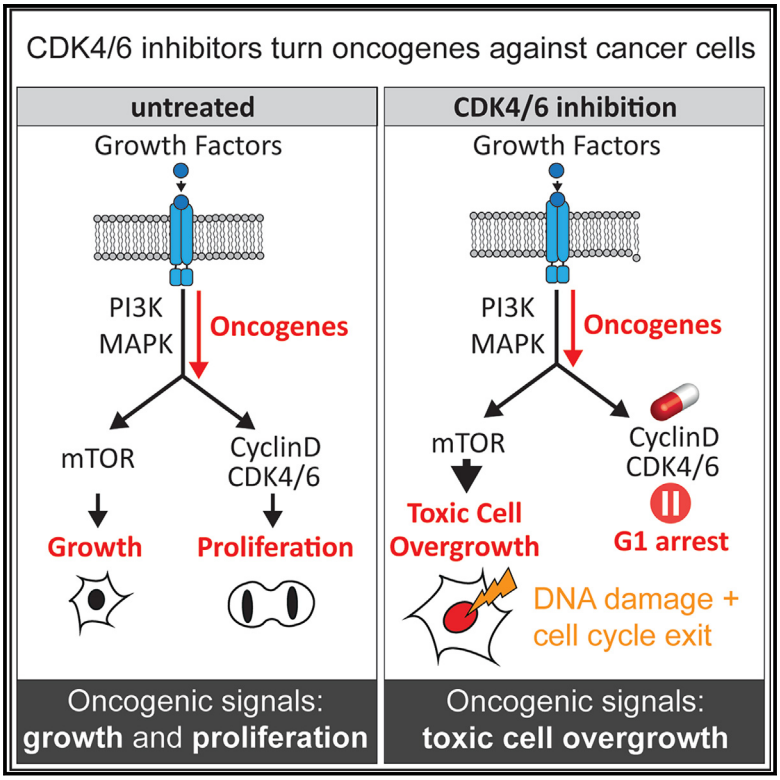

Highlights

- CDK4/6 inhibition causes mTOR-dependent cell overgrowth during the G1 arrest
- G1 overgrowth causes DNA damage and cell cycle withdrawal when the cell cycle resumes
- These effects are exacerbated by oncogenes and rescued by mTOR inhibition
- Specific drug combinations can enhance oncogene-specific overgrowth and toxicity

Authors

Reece Foy, Lisa Crozier, Aanchal U. Pareri, Juan Manuel Valverde, Ben Ho Park, Tony Ly, Adrian T. Saurin

Correspondence

a.saurin@dundee.ac.uk

In brief

Cell growth and the cell cycle must be coordinated to preserve cell viability. Foy et al. demonstrate that CDK4/6 inhibitors uncouple these two processes to drive excessive cellular overgrowth, DNA damage, and cell cycle exit. Oncogenic signals exacerbate these effects, likely contributing to cancer cell sensitivity to CDK4/6 inhibitors.

Foy et al., 2023, Molecular Cell *83*, 4047–4061
November 16, 2023
https://doi.org/10.1016/j.molcel.2023.10.020

CellPress

Molecular Cell

CellPress
OPEN ACCESS

Article

Oncogenic signals prime cancer cells for toxic cell overgrowth during a G1 cell cycle arrest

Reece Foy,[1,4] Lisa Crozier,[1,4] Aanchal U. Pareri,[1] Juan Manuel Valverde,[1] Ben Ho Park,[2] Tony Ly,[3] and Adrian T. Saurin[1,5,*]
[1]Cellular and Systems Medicine, Jacqui Wood Cancer Centre, School of Medicine, University of Dundee, Dundee DD1 9SY, UK
[2]Vanderbilt-Ingram Cancer Center, Vanderbilt University Medical Center, Nashville, TN 37232, USA
[3]Molecular Cell and Developmental Biology, School of Life Sciences, University of Dundee, Dundee DD1 5EH, UK
[4]These authors contributed equally
[5]Lead contact
*Correspondence: a.saurin@dundee.ac.uk
https://doi.org/10.1016/j.molcel.2023.10.020

SUMMARY

CDK4/6 inhibitors are remarkable anti-cancer drugs that can arrest tumor cells in G1 and induce their senescence while causing only relatively mild toxicities in healthy tissues. How they achieve this mechanistically is unclear. We show here that tumor cells are specifically vulnerable to CDK4/6 inhibition because during the G1 arrest, oncogenic signals drive toxic cell overgrowth. This overgrowth causes permanent cell cycle withdrawal by either preventing progression from G1 or inducing genotoxic damage during the subsequent S-phase and mitosis. Inhibiting or reverting oncogenic signals that converge onto mTOR can rescue this excessive growth, DNA damage, and cell cycle exit in cancer cells. Conversely, inducing oncogenic signals in non-transformed cells can drive these toxic phenotypes and sensitize the cells to CDK4/6 inhibition. Together, this demonstrates that cell cycle arrest and oncogenic cell growth is a synthetic lethal combination that is exploited by CDK4/6 inhibitors to induce tumor-specific toxicity.

INTRODUCTION

Identifying cell cycle vulnerabilities that distinguish cancer cells from healthy cells has been a long-term goal in cancer research.[1,2] A major breakthrough came with the development of CDK4/6 inhibitors, which have revolutionized the treatment of advanced hormone receptor-positive (HR+)/human epidermal growth factor receptor 2-negative (HER2−) breast cancer by increasing progression-free and overall survival when used in combination with hormone therapy.[3] The rationale for this combination is that blocking hormone receptor signaling inhibits the transcription of Cyclin D, the regulatory subunit of CDK4/6, thus producing a "double-hit" on Cyclin D-CDK4/6 activity, specifically in breast cancer cells that overexpress hormone receptors. This leads to an efficient arrest in G1 phase of the cell cycle because Cyclin D-CDK4/6 is required to phosphorylate retinoblastoma protein (Rb) and thereby activate E2F family transcription factors, which induce the expression of many genes required for S-phase.[4] Oncogenic signals also act to drive excessive Cyclin D production in many tumor types, and this has rationalized ongoing clinical trials to test whether inhibiting these signals alongside CDK4/6 can produce a similar double-hit to efficiently and specifically arrest tumor cell proliferation in breast and other tumor types.[3,5]

To facilitate wider use of these drugs, it is important to understand how they achieve specificity for tumor cells while only producing relatively mild toxicities in healthy tissues. This is thought to be due, at least in part, to the fact that tumor cells rely on the Cyclin D-CDK4/6 pathway for G1 progression more than some healthy cell types.[6,7] This might be due to the constant stimulation of the pathway by oncogenic signals, overexpression of Cyclin D/CDK4/CDK6, or loss/inhibition of tumor suppressors that restrain CDK4/6 activity (e.g., $p16^{INK4A}$ and p53/p21).[4] However, a crucial but poorly understood issue in the context of cancer therapy concerns not only how efficiently tumor cells arrest in G1 but also how these cells then respond to the arrest. A positive response is often associated with marked tumor regression that is sustained after chemotherapy has ceased, implying that tumor cells experience a cytotoxic response to these drugs and not simply a cytostatic G1 arrest. There are many ideas for why this could occur, including the notion that CDK4/6 inhibitors have intrinsic effects on tumor metabolism and extrinsic effects on the surrounding microenvironment to enhance anti-tumor immunity.[8,9] However, a major gap in our understanding concerns the questions of when, why, and how a pause in G1 transitions into a state of irreversible cell cycle exit, known as senescence.[10] It is critical to address these questions because they may help explain why tumors are more sensitive to these drugs than healthy cells, and this may ultimately help us better predict the most sensitive tumor types and/or the best drug combinations. We, therefore, set out to resolve these issues by building on our recent data demonstrating that a pause in G1, if held for

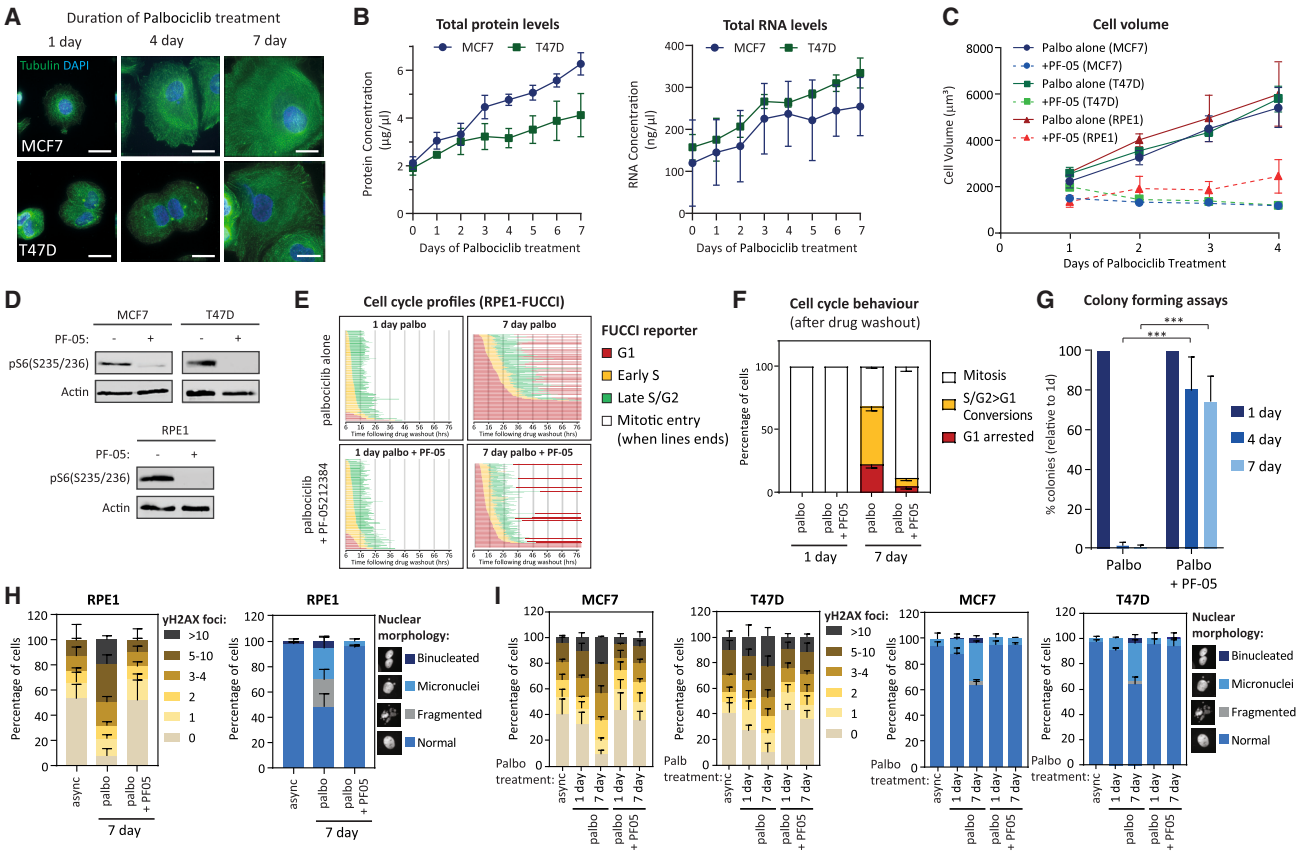

Figure 1. mTOR-dependent overgrowth during a G1 arrest drives DNA damage and cell cycle exit

(A and B) Immunofluorescence images (A) and protein/RNA concentration measurements (B) of MCF7 and T47D cells arrested in palbociclib for 0–7 days. Channel intensities in (A) are scaled differently between conditions to prevent tubulin saturation in small cells. Scale bars, 25 µm.

(C) Cell volume assays following 1–4-day palbociclib (palbo) treatment ± PF-05212384 (PF-05: 30 nM for RPE1, and 7.5 nM for MCF7/T47D; see Figures S1A and S1B for dose response). Graph shows mean data ± SD from three repeats.

(D) Western analysis of cells arrested in palbociclib for 1 day ± PF-05212384. Representative example of at least 3 repeats.

(E) Cell cycle profile of individual RPE1-FUCCI cells (each bar represents one cell) after washout from 1 or 7 days of palbociclib treatment ± PF-05212384. 150 cells analyzed at random from three experimental repeats.

(F) Quantifications of cell cycle defects from the single-cell profile plots displayed in (E). Bar graphs show mean − SD.

(G) Colony-forming assays in RPE1 cells treated with palbociclib ± PF-05212384 for 1, 4, or 7 days and then grown at low density without inhibitor for 10 days. Each bar displays mean data + SD from three experiments. Statistical significance was determined by Fisher's exact test (***$p < 0.0001$).

(H and I) Quantification of γH2AX-positive foci (left) and nuclear morphologies (right) following palbociclib treatment in p53-KO RPE1 cells (H) or MCF7/T47D cells (I). Cells were treated with DMSO (asynch) or palbociclib for 1 or 7 days ± PF-05212384 and then analyzed after drug washout for 48 h (RPE1 cells) or 72 h (MCF7/T47D). Graphs show mean data + SD from three experiments.

too long, downregulates various replisome components to cause DNA damage and long-term cell cycle withdrawal after release from the arrest.[11] The crucial question we sought to address was what happens during the G1 arrest that causes such widescale proteomic changes, ultimately causing problems during the subsequent cell cycle?

RESULTS

Cellular overgrowth following CDK4/6 inhibition causes genotoxic stress and cell cycle withdrawal

One clear effect of pausing cells for long periods in G1 is that they become progressively enlarged in size, as the total cellular protein and RNA continue to increase despite the cell cycle arrest. This occurs in non-transformed hTERT-RPE1 cells (RPE1) and HR+/HER2− breast cancer cells that are p53 proficient (MCF7) or p53 deficient (T47D) (Figures 1A–1C; see Crozier et al.[12]). This is broadly consistent with similar observations reported recently by others.[13–17] We sought to prevent this excessive growth during G1 so that we could test whether it was responsible for the downstream effects on DNA damage and long-term cell cycle exit. Excessive growth during G1 was phosphatidylinositol 3-kinase (PI3K)/mammalian target of rapamycin (mTOR) dependent because it was completely prevented by co-treatment with PF-05212384 (hereafter PF-05), a dual inhibitor of PI3K and mTOR[18] (Figures 1C, 1D, S1A, and S1B; note that phospho-S6 ribosomal protein is a critical downstream effector of mTOR/PI3K that regulates protein translation and cell

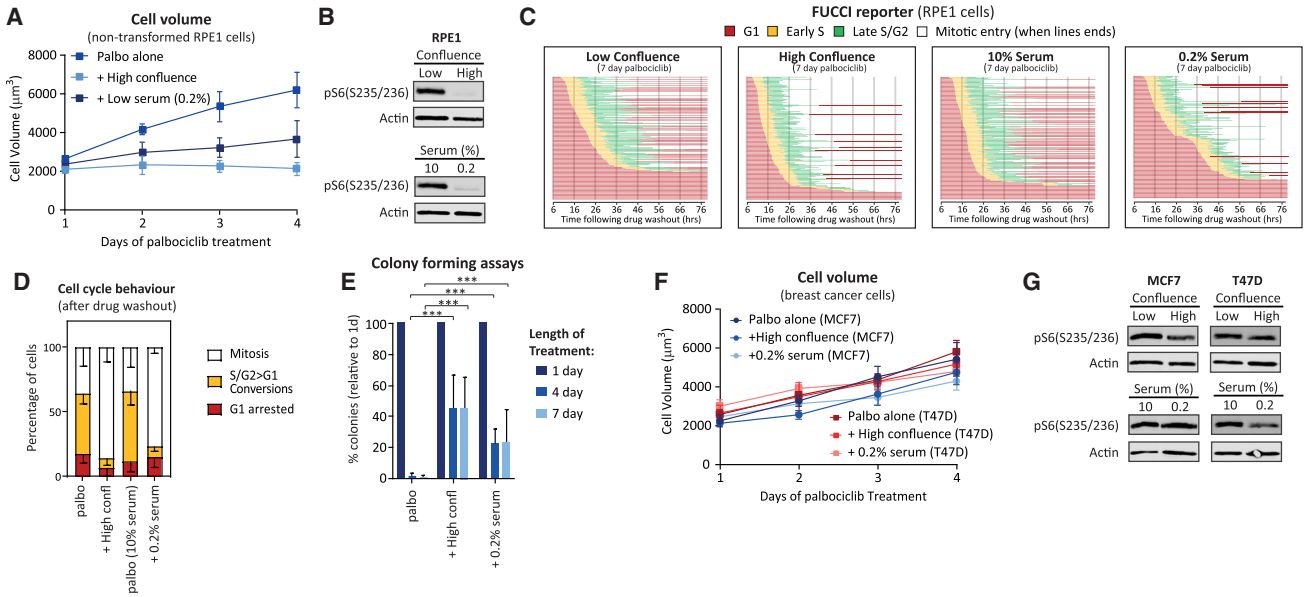

Figure 2. Serum withdrawal and contact inhibition can protect non-transformed cells from overgrowth and cell cycle exit following CDK4/6 inhibition

(A) Cell volume of RPE1 cells arrested in palbociclib for 1–4 days ± low serum or cultured at high confluence. Graphs show means ± SD from three repeats.

(B) Western analysis of RPE1 cells treated as in (A) but for 1 day. Representative example of at least 4 repeats.

(C) Cell cycle profile of individual RPE1-FUCCI cells (each bar represents one cell) after washout from 7 days palbociclib treatment ± low serum or cultured at high confluence. A total of 150 cells were analyzed at random from three experimental repeats.

(D) Quantifications of cell cycle defects from the single-cell profiles displayed in (C). Bar graphs show mean − SD.

(E) Colony-forming assays in RPE1 cells plated at high confluence or with low serum treated with palbociclib for 1, 4, or 7 days and then grown at low density without inhibitor for 10 days. Graphs show means + SD from three repeats. Statistical significance was determined by Fisher's exact test (***$p < 0.0001$).

(F) Cell volume assays in MCF7/T47D cells treated with palbociclib as described in (A). Graphs show means ± SD from three repeats.

(G) Western analysis of MCF7/T47D cells arrested with palbociclib but treated as described in (A). Representative example of 3 repeats.

size[19,20]). Single cell analysis with a FUCCI cell cycle reporter[21] demonstrates that when RPE1 cells are released from a prolonged G1 arrest, they struggle to re-enter the cell cycle, and the cells that do enter S-phase frequently revert back into G1 before reaching mitosis (Figure 1E), as demonstrated recently.[11] Importantly, both of these phenotypes were rescued when overgrowth was prevented with PF-05 (Figures 1E and 1F), which was associated with a dramatic improvement in long-term proliferation (Figure 1G). Cell cycle re-entry and progression were similarly improved in breast cancer cells following PF-05 treatment (Figures S1C and S1D).

Irreversible cell cycle withdrawal following CDK4/6 inhibition has recently been linked to replication stress as a result of impaired origin licensing and the progressive downregulation of replisome components during the G1 arrest.[11] This replication stress induces p53-dependent cell cycle withdrawal from G2 or, in the absence of p53, excessive DNA damage during mitosis, as the chromosomes are mis-segregated to produce γH2AX foci and gross nuclear abnormalities. In agreement with a crucial role for cell overgrowth in these phenotypes, combining PF-05 with CDK4/6 inhibitor rescued the increase in γH2AX foci and nuclear abnormalities following drug washout in p53-KO RPE1 cells (Figure 1H), which typically have the highest rates of damage,[11] and in breast cancer cells that are p53 proficient (MCF7) or deficient (T47D) (Figure 1I).

In summary, excessive cell growth during a G1 arrest drives permanent cell cycle withdrawal by restricting progression from G1 and causing DNA damage in the cells that do re-enter the cell cycle. Inhibiting PI3K/mTOR signaling can completely prevent this growth, DNA damage, and long-term cell cycle exit, thus explaining why mTOR activity is crucial to drive quiescent G1-arrested cells into senescence.[22–24] Therefore, mTOR status critically determines whether the arrest following CDK4/6 inhibition is cytotoxic or cytostatic. Accompanying papers by Crozier et al.[12] and Manohar et al.[25] in this issue of *Molecular Cell* report similar findings with distinct mTOR inhibitors and explain mechanistically how overgrowth causes proteome remodeling, osmotic stress, replication stress, and defective DNA damage repair to cause permanent cell cycle exit. Here, we seek to examine the upstream signals that drive this overgrowth and explore whether these vary between cell types, since this would be predicted to have a crucial effect on outcome following CDK4/6 inhibition.

Cancer cells are sensitized to overgrowth and cell cycle withdrawal following CDK4/6 inhibition

The levels of cell growth and mTOR activity are determined by the balance of growth promoting and growth repressing signals, which, importantly, depends on both cell context and cell type. In non-transformed epithelial cells, growth factor

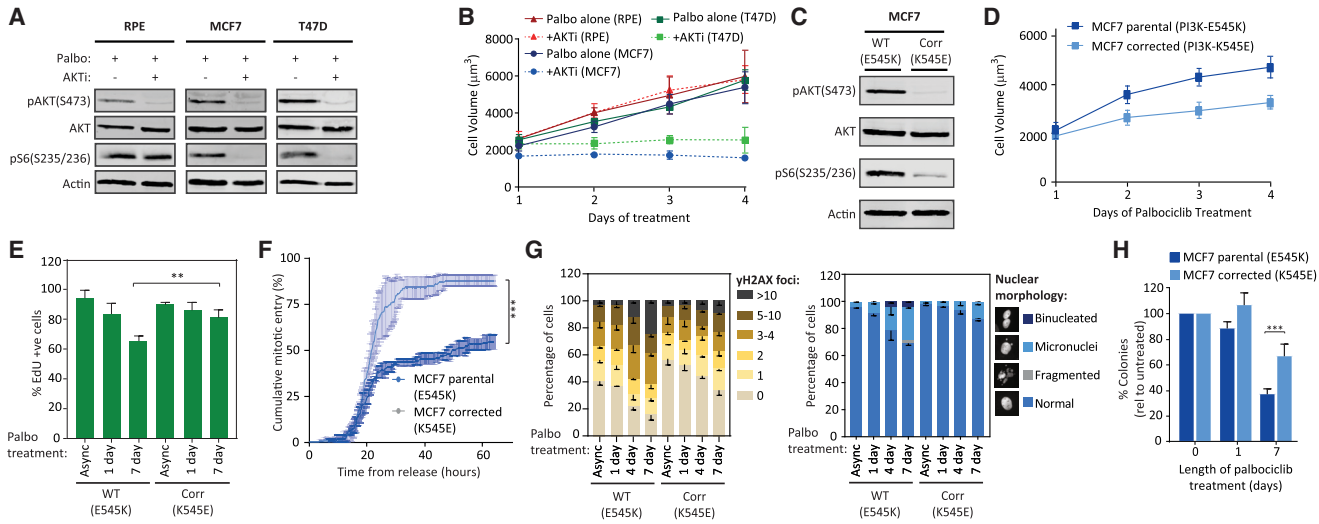

Figure 3. G1 overgrowth and cell cycle exit are driven by oncogenic signals in cancer cells

(A) Western analysis of indicated cells arrested in palbociclib for 1 day ± MK2206 (AKTi). Representative example of 3 repeats.

(B) Cell volume assays of indicated cell lines arrested in palbociclib for 1–4 days ± MK2206 (AKTi). Graphs show mean data ± SD from three repeats.

(C) Western analysis of indicated MCF7 cells, with/without a PI3K-E545K mutation,[28] arrested in palbociclib for 1 day. Representative example of 3 repeats.

(D) Cell volume of indicated MCF7 cells arrested in palbociclib for 1–4 days. Graphs show means ± SD from three repeats.

(E) Percentage of indicated MCF7 cells incorporating EdU over 72 h following washout from 1- or 7-day palbociclib arrest. Graphs show means + SD from three repeats, and at least 100 cells were quantified per experiment. Statistical significance was determined by Fisher's exact test (***$p < 0.0001$).

(F) Cumulative mitotic entry in indicated MCF7 cells following washout from 7-day palbociclib arrest. A total of 50 cells were quantified at random per experiment, and graph displays mean ± SEM from three experiments. Statistical significance was determined by Mann-Whitney test (***$p < 0.0001$).

(G) Quantification of γH2AX-positive foci (left) and nuclear morphologies (right) following palbociclib treatment in indicated MCF7 cells. Cells were treated with DMSO (asynch) or palbociclib for 1 or 7 days and then analyzed 72 h after drug washout. Graphs show means − SD from three experiments.

(H) Colony-forming assays in indicated MCF7 cells treated with palbociclib for indicated times and then grown at low density without inhibitor for 10 days. Graphs show means + SD from 4 experiments. Statistical significance was determined by Fisher's exact test (***$p < 0.0001$). The MCF7 cells used in (C)–(H) were parental cells (PI3K-E545K) or cells in which the oncogenic mutation has been corrected back to wild type (corrected PI3K-K545E), as published previously.[28]

signaling stimulates mTOR to drive cell growth and proliferation; however, upon cell-cell contact, these signals are rapidly shut down by contact inhibition of proliferation.[26] Figures 2A–2E demonstrate that both serum withdrawal and cell-cell contact can inhibit mTOR and protect RPE1 cells from toxic overgrowth during a G1 arrest, thereby limiting cell cycle exit and restoring long-term proliferation following release from the arrest. This is in sharp contrast to breast cancer cells, which continue to activate mTOR and grow during a G1 arrest, despite culturing in low serum or at high confluence (Figures 2F and 2G). Therefore, two pervasive hallmarks of cancer—loss of contact inhibition and growth factor independence—facilitate the overgrowth of cancer cells following CDK4/6 inhibition.

We hypothesized that the persistent mTOR-dependent growth in cancer lines was driven by oncogenic mutations, which in the case of HR+/HER2− breast cancer cells, are often activating PI3K mutations (PI3K-E545K in MCF7 or PI3K-H1047R in T47D), which signal to mTOR via AKT kinase (also known as protein kinase B). In agreement with this hypothesis, inhibiting AKT with the allosteric inhibitor MK2206[27] deactivated AKT in all cell types but only prevented mTOR activity and growth in the breast cancer lines (Figures 3A and 3B). This could also be achieved by reverting the oncogenic PI3K-E545K mutation in MCF7s back to wild type[28] (Figures 3C and 3D), which was associated with better cell cycle progression, decreased DNA damage following drug release, and enhanced long-term proliferation (Figures 3E–3H). Note that most of the replication stress-induced DNA damage occurs after mitosis when chromosomes are incorrectly segregated.[11] Therefore, the fact that oncogene reversion almost doubles the number of cells reaching mitosis (Figure 3F) but still reduces the overall DNA damage (Figure 3G) implies that replication stress is markedly reduced in these cells, most likely because of their restricted growth during G1. In agreement, in an accompanying manuscript by Crozier et al.,[12] we demonstrate that replication fork speed is slowed when enlarged CDK4/6-inhibitor-treated cells are released into S-phase but not when mTOR inhibitor is used to prevent overgrowth during the G1 arrest. Interestingly, although growth could not be prevented in RPE1 cells by AKT inhibition, it could be fully suppressed by combined inhibition of mitogen-activated protein kinase kinase (MEK) and AKT, and this was associated with improved cell cycle progression following drug washout (Figure S2). This could reflect the dependence on upstream growth factors that stimulate both MEK/PI3K pathways and/or on the oncogenic KRAS mutation present in RPE1 cells.[29,30]

In summary, oncogenic signals drive excessive growth during a G1 arrest, and this leads to DNA damage and long-term cell cycle withdrawal when cells are released from the arrest.

CellPress
OPEN ACCESS

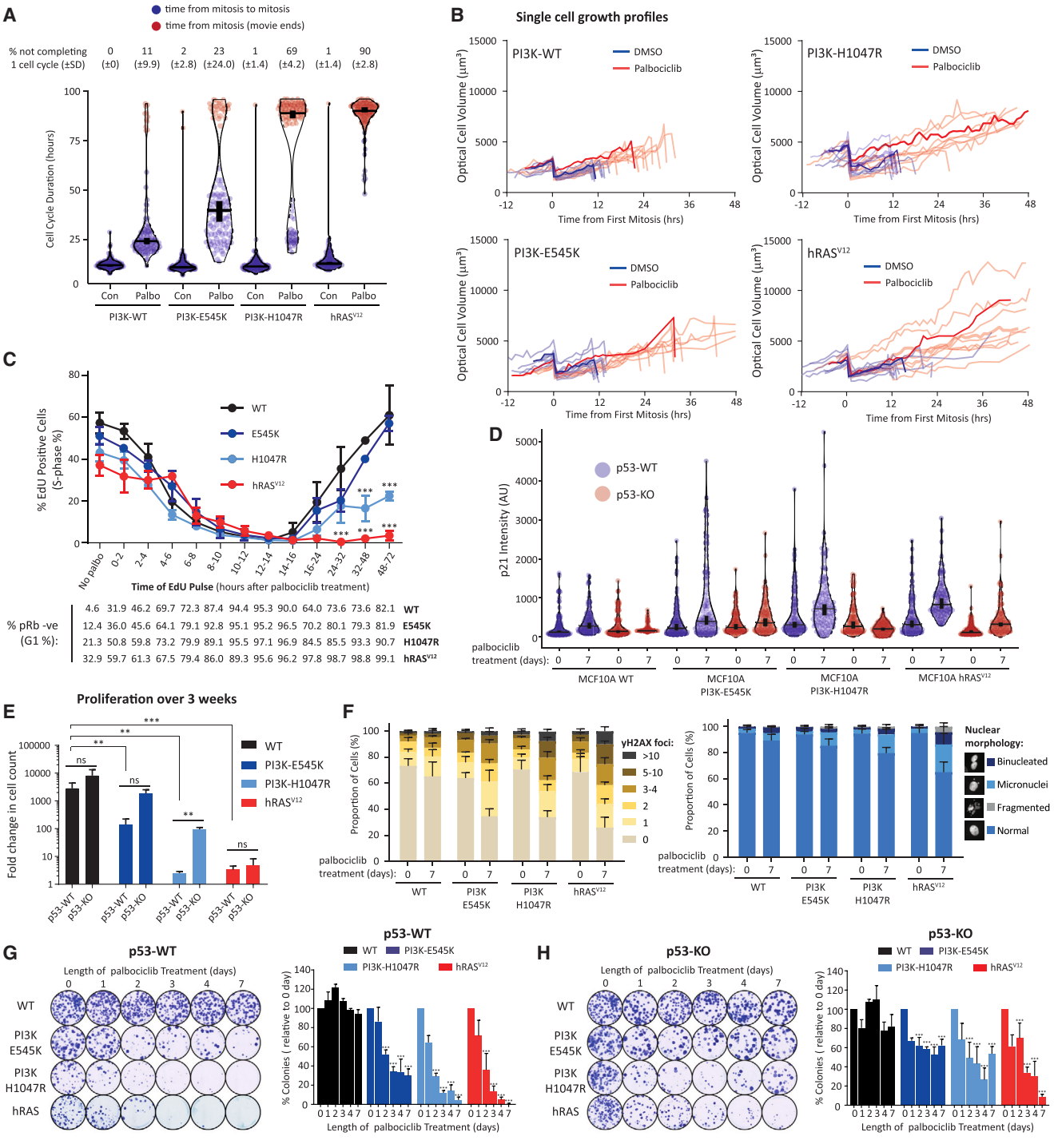

Figure 4. Oncogenes sensitize MCF10A cells to CDK4/6 inhibition

(A and B) MCF10As, with/without indicated oncogenes, treated with DMSO or palbociclib (palbo) for 4 days and analyzed by holographic microscopy to quantify (A) cell cycle duration and (B) single-cell optical volume. Data in (A) are from 100 cells from 2 experiments. Horizontal bars show median, and vertical bars show 95% confidence intervals. In (B), a typical single-cell volume trace is shown in blue (vehicle treated) or red (palbociclib treated). Random cell volume traces from 10 cells from 2 experiments are shown in light blue/red.

(C) Indicated MCF10A cells treated with palbociclib and EdU added for indicated time periods to calculate the percentage of S-phase cells during these time periods. pRb (S807/811) staining (pRb) indicates the percentage of G1 cells during the same time periods. Graphs show means ± SEM from 3 repeats (EdU) or 2 repeats (Rb-pSer807/811). Statistical significance was determined by unpaired t tests (***$p < 0.0001$).

(legend continued on next page)

Oncogenic mutations sensitize non-transformed breast epithelial cells to CDK4/6 inhibition

We next addressed whether non-transformed breast epithelia could be sensitized to CDK4/6 inhibition by introducing oncogenic mutations. We used MCF10A with an endogenous PI3K-E545K or PI3K-H1047R knockin mutation[31] or MCF10A with a tamoxifen-inducible hRAS-G12V mutant ($hRAS^{V12}$).[32] Growth following CDK4/6 inhibition was enhanced in the presence of the oncogene; however, this growth plateaued after 2 days in all cells except the MCF10A-$hRAS^{V12}$ cell line, which experienced significant overgrowth during the 4-day treatment (Figure S3A; note that tamoxifen was added at 250 nM for all experiments involving the $hRAS^{V12}$ line). The plateau in net growth was likely related to an inefficient cell cycle arrest because all cells, except MCF10A-$hRAS^{V12}$, were able to continue to proliferate to different extents over the 4-day period of CDK4/6 inhibition (Figure S3B).

To determine whether this reflected cell cycle delays in all cells or a penetrant G1 arrest in only a subset of cells, we turned to single-cell assays to simultaneously measure cell cycle length (time from one mitosis to the next mitosis) and cell volume. Figure 4A demonstrates that all vehicle-treated MCF10A cell lines had a 12-h cell cycle length, during which time cell volume increased linearly (Figure 4B; blue lines). The average mitotic volumes and growth rates were not significantly different between cell types (Figures S3C and S3D). Following CDK4/6 inhibition, cell cycle length was extended in all cells, but this extension was longer in cells expressing oncogenic mutants (Figure 4A). The longest cell cycles were observed in $hRAS^{V12}$-expressing cells, of which 90% failed to complete a full cell cycle within the 4-day imaging window. A striking effect of these cell cycle delays was that they allowed cells to continue to grow in size (Figure 4B; red lines). This growth occurred linearly throughout the period of delay, and growth rates were not significantly different between the oncogenic mutant lines (Figures 4B and S3C). The net effect was that when cells entered mitosis following a cell cycle delay, they did so with a larger cell volume (Figure S3D).

We next used EdU pulse assays to mark S-phase cells[33] and therefore determine at what stage the cell cycle was delayed following CDK4/6 inhibitor treatment. A 2-h pulse of EdU in asynchronous parental MCF10A cells demonstrated that 57% of the cells were in S-phase during the pulse, and only 5% of the cells were phospho-Rb (S807/811) negative (pRB-ve), indicating very short G1 phases (Figure 4C). Following palbociclib treatment, the percentage of S-phase cells decreased over time, and this was mirrored by an increase in the pRB-ve G1 population, which persisted for 14 h. After this time, cells started to accumulate again in S-phase, demonstrating that palbociclib treatment can delay MCF10A cells in G1 for up to 14 h. Importantly, oncogene expression elevated the proportion of untreated MCF10A cells in G1, and palbociclib treatment induced longer G1 delays in these cells, with most $hRAS^{V12}$- and PI3K-H1047R-expressing cells remaining arrested in G1 for the 4-day period. This correlated well with the extended cell cycle duration observed in these cells (Figure 4A). In summary, CDK4/6 inhibition delays G1 progression in MCF10A cells, and this allows cells to reach a larger size. The oncogene-expressing cells experience longer G1 delays and, therefore, reach larger overall sizes.

We hypothesized that the overgrowth in oncogenic MCF10A cells would lead to DNA damage and p53/p21-dependent cell cycle withdrawal. In agreement, p21 intensity was elevated in cells treated with CDK4/6 inhibitor for 7 days, this was higher in oncogene-expressing cells, and this was associated with an inhibition of proliferation over 3 weeks of treatment (Figures 4D, 4E, and S3E). To examine this further, we generated p53 or p21 knockout (KO) MCF10A cells using CRISPR-Cas9 (Figure S3F). In p53-KO cells, p21 induction was suppressed, and cells proliferated better over this treatment period (Figures 4D, 4E, S3F, and S3G). However, cells that continued to proliferate in this situation experienced high levels of DNA damage after only 1 week of treatment, most likely due to catastrophic mitoses in enlarged cells (Figures 4F and S3H).[11] Strikingly, MCF10A cells that exhibited slower proliferation in the presence of CDK4/6 inhibitor for up to 1 week could fully recover long-term proliferation when the drug was removed (Figure 4G). This indicates that the cell cycle delays and modest increase in size observed in wild-type MCF10A cells do not cause permanent cell cycle exit in this non-transformed epithelial line. This was in sharp contrast to all oncogene-expressing MCF10A cells, which dramatically lose long-term proliferative potential after as little as 3 days of CDK4/6 inhibitor treatment (Figure 4G). Long-term proliferation was partially rescued by p53 knockout (Figure 4H), implying that oncogene-dependent cell overgrowth causes p53-dependent cell cycle withdrawal.

Oncogenic mutations elevate p21 levels during G1 to improve a CDK4/6 inhibitor arrest in MCF10A cells

The ability of oncogenes to extend the G1 arrest following CDK4/6 inhibition is surprising, given the established role of oncogenic signals in driving cell growth, Cyclin D production, and G1 progression. To understand this better, we performed quantitative proteomics to analyze how the concentration of G1 regulators changed as MCF10A cells grew during a G1 arrest (see STAR Methods). To analyze G1 protein concentration in all MCF10A lines, we required a method that would hold wild-type MCF10A cells in G1 for longer. Therefore, we treated MCF10A lines with CDK4/6 inhibitor for 24 h and then switched to the CDK2/4/6

(D) p21 intensities in indicated p53-WT/KO MCF10A cells ± palbociclib for 1 week. A total of 50 cells per condition per experiment from 2–3 experimental repeats. Horizontal bars show median, and vertical bars show 95% confidence intervals.
(E) Mean fold change in cell count (±SEM) after 3-week palbociclib treatment in indicated p53-WT/KO MCF10A cells. Data from 3–4 experimental repeats. Statistical significance was determined by unpaired t tests (**$p < 0.005$; ***$p < 0.0001$).
(F) Quantification of γH2AX-positive foci (left) and nuclear morphologies (right) in indicated MCF10A cells treated with DMSO (0 days) or palbociclib for 7 days and then analyzed 72 h after drug washout. 50 cells were analyzed per condition per experiment. Graphs show means + SD from three experiments.
(G and H) Colony-forming assays in indicated p53-WT (G) or P53-KO (H) MCF10A cells treated with palbociclib for up to 7 days and then grown at low density without inhibitor for 10 days. Graphs show mean + SD from 3 experiments. Statistical significance between each palbociclib time point and the asynchronous 0-day control was determined using Fisher's exact test (*$p < 0.05$; ***$p < 0.0001$). The thick vertical lines in the violin plots in (A) and (D) represent a 95% CI around the median (horizontal lines), which can be used for statistical comparison of multiple time points/treatments by eye (see STAR Methods).

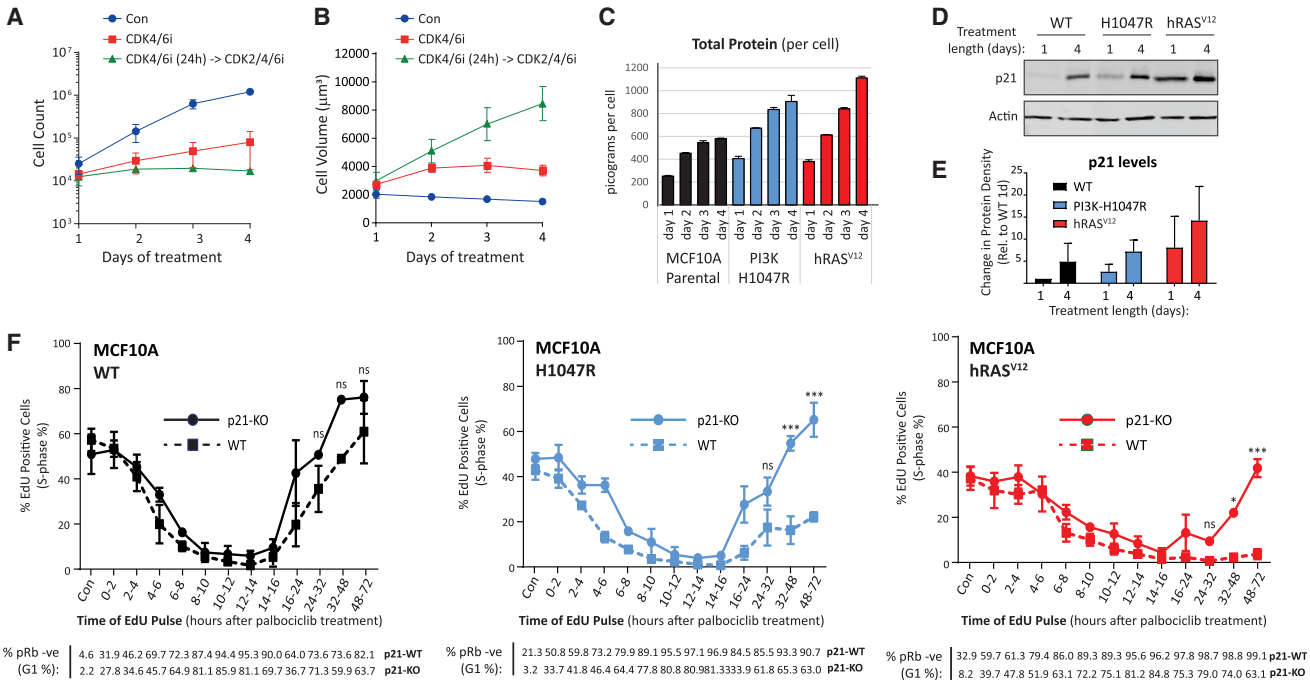

Figure 5. CDK4/6 inhibition arrests oncogenic MCF10A cells more efficiently due to p21 upregulation during the G1 arrest

(A and B) Cell count (A) and cell volume (B) of MCF10A cells treated as indicated for 1–4 days (Con, DMSO; CDK4/6i, palbociclib; CDK2/4/6i, PF-06873600). The CDK2/4/6i-treated cells were pre-treated with CDK4/6i for the first 24 h to arrest in G1 before being switched to CDK2/4/6i. Graphs show means ± SD from 3–7 repeats.

(C) Total protein per cell from indicated MCF10A cells treated with palbociclib for 24 h (1 day) and then switched into CDK2/4/6 inhibitor (PF-06873600) for the remaining treatment times (2–4 days). Graphs show means ± SD from three repeats.

(D) Western analysis of MCF10A cells treated with palbociclib for 1 day and then switched into the CDK2/4/6 inhibitor PF-06873600 for 3 additional days (4 days). Cell lysates were equalized by total protein concentration prior to blotting.

(E) Quantification of the 3 repeats from (D). Changes relative to wild-type (WT) 1-day treatment.

(F) Indicated MCF10A cells treated with palbociclib, and EdU added for indicated time periods to calculate the percentage of S-phase cells during these time periods. pRb (S807/811) staining indicates the percentage of G1 cells during the same time periods. Graphs show means ± SEM from 3 repeats (EdU) or 2 repeats (Rb-pSer807/811). Statistical significance was determined using unpaired t tests (*$p < 0.05$; ***$p < 0.0001$). The MCF10A p21-WT plots are displayed from Figure 4C to allow comparison (these experiments were performed at the same time).

inhibitor PF-06873600[34,35] at 1 µm to additionally block CDK2 activity and restrict S-phase entry. This strategy improved the G1 arrest, inhibited proliferation over 4 days, and allowed cells to become enlarged (Figures 5A, 5B, and S4A). We analyzed protein copy numbers per cell during 1 to 4 days of this arrest, and the entire data are presented in Table S1. Total protein content per cell (as measured by mass spectrometry) was higher in oncogenic cells, and this increased during the 4-day period of growth, as expected (Figure 5C). The majority of established G1 regulators were detected, and the estimated protein concentrations (in parts per million [ppm]) for these regulators are displayed in Figures S4B–S4D. Compared with wild type, oncogenic growth reduced the concentrations of the cell cycle activators CDK2, CDK4, and CDK6, which could contribute to the enhanced G1 delays in oncogenic cells. Perhaps more importantly, however, the concentration of the CDK inhibitor p21 was increased in oncogenic cells by day 1 of treatment and then increased further during the arrest. These effects were also confirmed by western blot analysis (Figures 5D and 5E).

Progression through G1 is determined by the balance of G1 activators and inhibitors, and this balance shifts toward the activators as cells grow in size. This ability to "grow through" a G1 arrest is thought to form the basis of a cell-size checkpoint that ensures that cells reach an optimal size before progressing into S-phase.[14,36–39] A prediction of this model is that by inhibiting G1>S activators, such as CDK4/6, cells must then grow larger to overcome the G1/S inhibitors. In support of this hypothesis, increasing concentrations of palbociclib lead to progressively longer G1 delays in RPE1-FUCCI cells, and this is associated with progressive increases in cell volume when these cells reach mitosis (Figures S5A and S5B). Similar data were recently reported by others.[13,17] Growth is facilitating the G1>S transition in this situation because PF-05 treatment prevented cells from progressing from G1 in the presence of low-dose palbociclib (Figure S5C). Cell growth is similarly important for MCF10A cells to bypass a CDK4/6-inhibitor-induced arrest in G1 because PF-05 treatment produced an efficient palbociclib arrest for up to 4 days (Figure S5D). Therefore, we hypothesized that the elevated p21 induction in oncogenic MCF10A cells arrested in palbociclib could restrain the capacity of these cells to bypass a G1 arrest through cell growth because p21 also scales during that growth phase

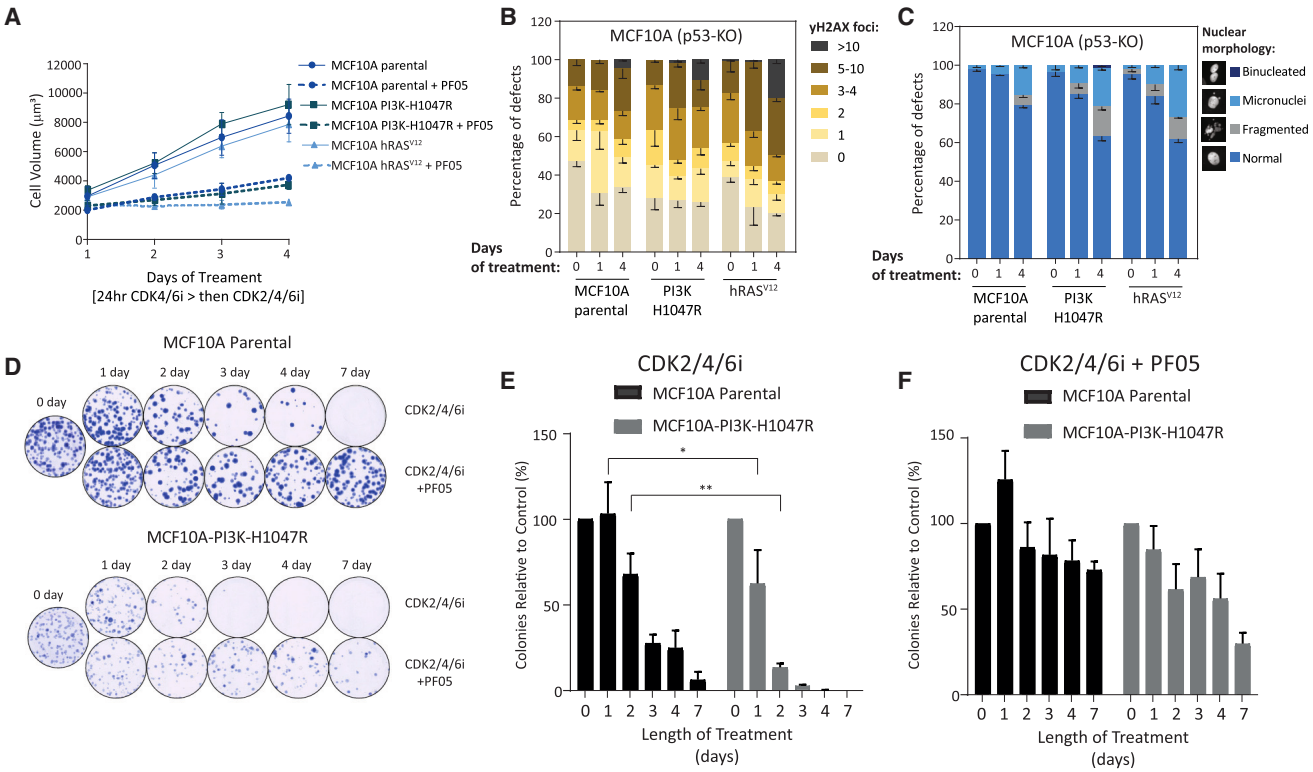

Figure 6. Oncogenes sensitize MCF10A cells to a prolonged CDK2/4/6 inhibitor arrest

(A) Cell volume of indicated MCF10A cells treated with CDK4/6i (palbociclib) for 1 day and then transferred into CDK2/4/6i (PF-06873600) for the remaining 3 days of treatment. Assays performed ± PF-05212384. Graph shows mean ± SD from at least three repeats, except MCF10A parental cells without PF05 with 7 repeats (these data are duplicated from Figure 5B for comparison; experiments were performed at the same time).

(B and C) Quantification of γH2AX-positive foci (B) and nuclear morphologies (C) in indicated MCF10A cells treated with DMSO (0 day), palbociclib for 1 day, or palbociclib for 1 day and then switched into PF-06873600 (CDK2/4/6i) for another 3 days (4 days). Drugs were washed out for 72 h before quantification. Graphs show means + SD from three repeats.

(D–F) Colony-forming assays with indicated MCF10A cells treated with CDK4/6i (palbociclib) for 24 h before replacing with the CDK2/4/6 inhibitor PF-06873600. Total treatment lasted from 0–7 days and were performed ± PF-05 for the whole treatment period, as indicated. Drugs were then removed, and cells were allowed to form colonies for 10 days. Statistical significance was determined with unpaired t tests (*$p < 0.05$; **$p < 0.005$). Data show mean of 3 repeats + SEM.

(Figures 5D, 5E, and S4D). In agreement, EdU pulse experiments in p21-KO MCF10A cells demonstrate improved S-phase entry following palbociclib treatment, especially in the oncogenic MCF10A cells (Figures 5F and S4E). In summary, palbociclib can delay G1 progression in MCF10A cells, and this delay is extended by oncogenic signals as a result of enhanced p21 induction during the G1 arrest. We propose that growth is able to overcome a G1 arrest by producing an excess of G1/S activators, but if p21 levels rise too highly during this growth phase, then cell cycle progression is still effectively prevented. It is unclear why oncogenic MCF10A cells have higher p21 levels and, therefore, are unable to grow and efficiently bypass a palbociclib-induced G1 arrest. In an accompanying paper by Crozier et al.[12] in this issue of *Molecular Cell*, we explain how p21 is induced during G1 overgrowth by osmotic stress, which is associated with differential proteome scaling. Proteomic analysis indicated that oncogenic cells have some differences in their scaling behavior (Figure S4F; Table S2) and overall increases in their protein content (Figure 5C), both of which may contribute to the stronger p21 induction. Alternatively, oncogene-induced replication stress could elevate basal p21 transcription, leading to enhanced p21 protein production during G1-phase growth.

Oncogenic mutations sensitize non-transformed breast epithelial cells to CDK2/4/6 inhibition

We next wondered whether oncogenes sensitized MCF10A cells mainly by improving the cell cycle arrest to enhance overgrowth. To address this, we asked whether oncogenes would also sensitize MCF10A cells to a more prolonged CDK2/4/6 inhibitor arrest, which allowed wild-type MCF10A cells to arrest and become enlarged (Figures 5A and 5B). This is important because this drug is in clinical development to help overcome CDK4/6 resistance.[34,40] We performed the sequential CDK4/6 inhibition (24 h), followed by CDK2/4/6 inhibition, to arrest MCF10As in G1 for up to 4 days, before releasing cells into S-phase. Figures 6A–6E and S6 demonstrate that oncogenes do not significantly enhance the level of growth under these conditions, but they do enhance the level of DNA damage observed 48 h after drug release, and, importantly, they also cause a reduction in

long-term proliferation. The enhanced cell cycle withdrawal is fully growth-dependent because it is prevented by the addition of PF-05 to inhibit overgrowth during the arrest (Figure 6F). Therefore, oncogenes can sensitize non-immortalized MCF10A cells to overgrowth-mediated DNA damage and cell cycle exit following CDK2/4/6 inhibition. This could be due to abnormal proteome scaling causing enhanced toxicity during the G1 growth phase and/or oncogene-induce replication stress[41] exacerbating the problems experienced by large cells during S-phase.

Rationalizing drug combinations that enhance oncogene-specific toxicity

We hypothesized that oncogenes would drive mTOR activity via different routes, either via MEK/MAPK or PI3K/AKT or via both pathways. This could provide an opportunity to use combination treatments that specifically prevent overgrowth and toxicity in healthy cells but not cancer cells. To explore these concepts, we chose to use a non-transformed retinal pigment epithelial cell line, ARPE19, which has been retrovirally transduced to express different dominant oncogenic mutants (AKT^{myr}, MEK^{DD}, or $hRAS^{V12}$ in a p53 mutant background; see STAR Methods for full details of oncogenes). We specifically chose these cells because they had previously been transduced with TERT, $mTP53^{DD}$, CCND1, and $CDK4^{R24C}$, which promotes CyclinD1/CDK4-dependent G1 progression to inhibit oncogene-induced senescence.[42] Therefore, we hypothesized that this would lead to strong CDK4/6 dependence. ARPE19 cells were sensitive to CDK4/6 inhibition because they stopped proliferating within 12 h of palbociclib treatment, and the subsequent G1 arrest was well maintained for up to 4 days (Figures 7A and S7A). Oncogenes enhanced the level of overgrowth during the G1 arrest to different extents, and this was mTOR dependent since it was blocked by PF-05 treatment (Figures 7B and S7B). The overgrowth enhanced DNA damage following CDK4/6 inhibitor washout in all cell lines, but this damage was highest following p53 mutation in the presence of oncogenes, especially AKT^{myr} and $hRAS^{V12}$ (Figures 7C and S7C–S7E). The overgrowth caused long-term cell cycle exit, but this was attenuated in p53 mutant cells (Figure S7F). This is consistent with similar effects in MCF10A (Figure 4) and RPE1 cells,[11] demonstrating that overgrowth commonly leads to DNA damage and p53-dependent cell cycle withdrawal.

MEK inhibition reduced mTOR activity and growth in all lines, implying that this pathway is commonly needed for growth in ARPE19 cells (Figures 7D and 7E). In contrast, AKT inhibition with the allosteric inhibitor MK2206 (labeled $AKTi^{(allo)}$) inhibited growth and mTOR activation in most cell lines, except the AKT^{myr} line (Figures 7D and 7E). This was expected since AKT^{myr} lacks the pleckstrin homology (PH) domain to which MK2206 binds to inhibit membrane binding[43] and is instead constitutively bound to the plasma membrane. This insensitivity to MK2206 can be exploited to enhance oncogene-specific DNA damage because MK2206 combined with CDK4/6 inhibitor protected parental cells from DNA damage, but not AKT^{myr} cells (Figures 7F and S7G). This effect was not observed with the ATP-competitive AKT inhibitor capivasertib (labeled $AKTi^{(ATP)}$), which protected both cell lines. Interestingly, however, capivasertib was unable to prevent growth or mTOR activity in $hRAS^{V12}$ cells (Figures 7D and 7E); therefore, combining it with CDK4/6 inhibitor could protect parental, but not $hRAS^{V12}$, cells (Figure S7H). Together, these data illustrate how knowledge of the specific coupling between oncogenes and mTOR can be harnessed to rationalize drug combinations that enhance oncogene-specific toxicity following a G1-arrest.

DISCUSSION

Cell growth must be tightly coupled to cell cycle progression to preserve cell and organismal viability. We demonstrate here that CDK4/6 inhibitors uncouple these two key processes to induce cancer cells to withdraw from the cell cycle. The reason for this is that oncogenic signals stimulate both cell growth and cell cycle entry, but when the cell cycle is halted in G1 by CDK4/6 inhibition, these oncogenic signals induce excessive cell overgrowth that soon becomes toxic. An accompanying article in this issue of *Molecular Cell* reports similar findings with CDK7 inhibition,[44] implying that different cell cycle drugs may drive senescence via similar mechanisms. The concept that hyper-mitogenic signals can drive overgrowth and senescence in arrested cells was proposed nearly 2 decades ago[45] but has received little attention since.[46] This is especially surprising since it could explain how general cell cycle inhibitors can produce tumor-specific effects, an age-old problem in cancer research that has, in contrast, received considerable attention over the years. If oncogenes make tumor cells more vulnerable to a G1 cell cycle arrest, then efficiently arresting all cells in G1, for defined periods of time, may lead to cancer-specific overgrowth, DNA damage, and senescence. It will be important to compare the rates of growth in different G1-arrested cell types *in vivo* because if these differ, then modified dosing schedules may help optimize cancer-specific cell overgrowth, toxicity, and DNA damage.

There are many different factors that contribute to toxicity and DNA damage in enlarged G1-arrested cells. First, the overgrowth itself causes gross remodeling of the proteome. Some compartments scale with size, whereas others subscale or superscale.[12,15,47] Second, this atypical scaling induces stress responses that impact subsequent cell cycle progression. In yeast, G1-arrested cells overgrow, and this induces an environmental stress response that is associated with cytoplasmic dilution.[15] In human cells, cytoplasmic dilution may also occur following CDK4/6 inhibition, leading to decreased macromolecular crowding.[15] Consistent with this model, Crozier et al.[12] demonstrate that overgrowth triggers an osmotic stress response that is associated with increased intracellular osmolyte concentrations. This osmotic stress response causes p21 induction via a p38-mediated pathway, resulting in delayed and attenuated exit from G1 when CDK4/6 inhibitors are removed. Third, enlarged cells can escape the G1 arrest, but these cells experience significant replication stress during the proceeding S-phase.[11,12] Fourth, the DNA damage response is also impaired in enlarged cells, and the DNA itself may be prone to damage.[25] As a result of these replication-associated problems, p21 protein is induced again as cells enter G2, causing further cell cycle withdrawals.[12] Finally, cells that fail to exit the cell cycle from G2, in particular p53-deficient cells that cannot induce p21, enter mitosis and

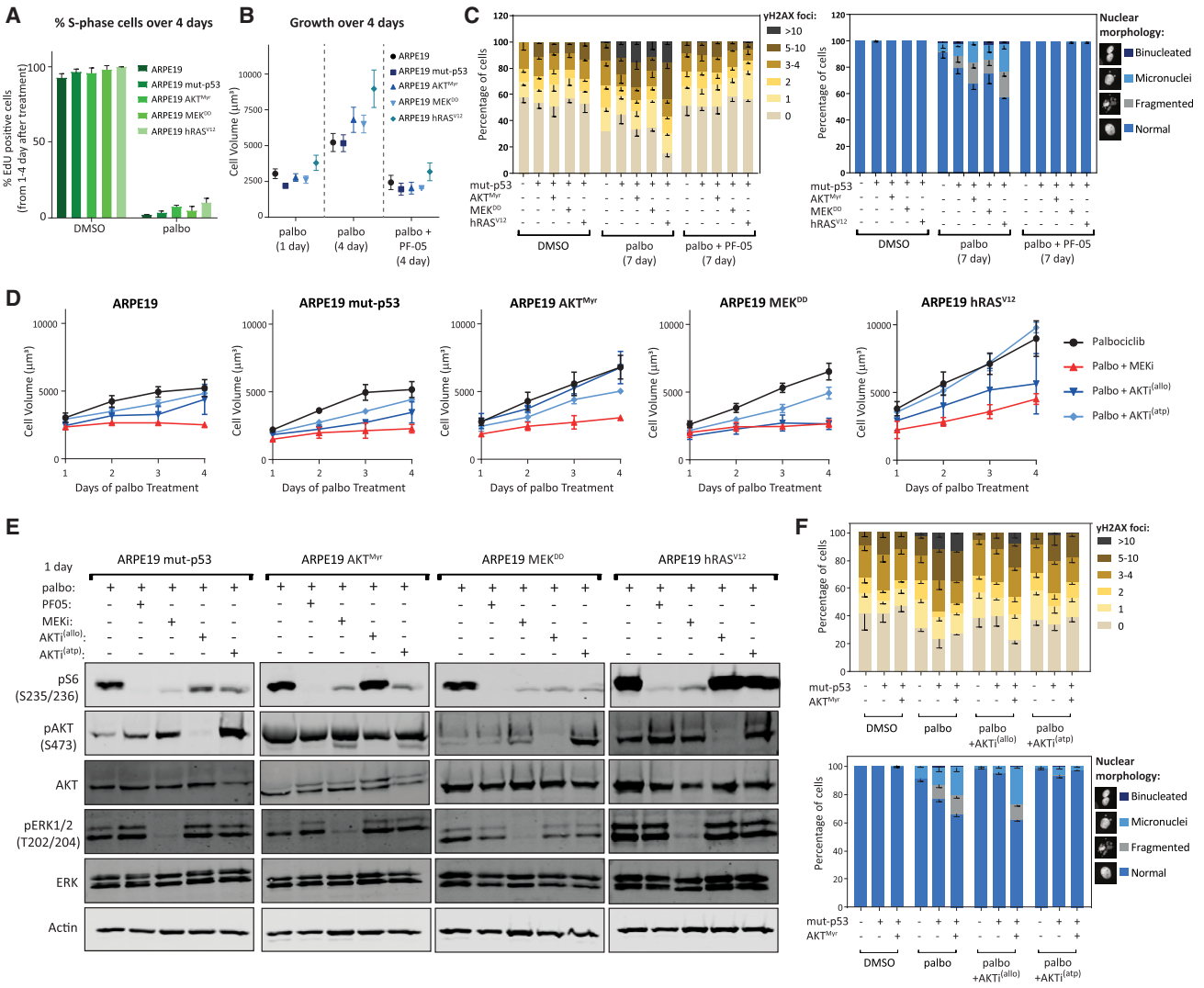

Figure 7. Enhancing oncogene-specific overgrowth and toxicity using tailored drug combinations

(A) Indicated ARPE19 cells were treated with palbociclib, and EdU added at day 1 for 3 further days to calculate the percentage of S-phase cells during the CDK4/6 inhibitor arrest. Data show mean + SD from three repeats, and at least 500 cells were analyzed per condition.

(B) Cell volumes of indicated ARPE19 cells treated with palbociclib for 1 day, 4 days, or 4 days + PF-05212384. Graph shows means ± SD from three repeats.

(C) Quantification of γH2AX-positive foci (left) and nuclear morphologies (right) in indicated ARPE19 cells treated with DMSO or palbociclib for 7 days ± PF-05212384 and then analyzed 72 h after drug washout. Graphs show means − SD from three repeats.

(D) Cell volume of indicated ARPE19 cells after 1–4 days of palbociclib treatment ± indicated growth inhibitors (MEKi, PD-0325901; AKTi$^{(allo)}$, MK2206; capivasertib, AKTi$^{(atp)}$). Graph shows mean data ± SD from three repeats.

(E) Western analysis of indicated cell lines arrested in palbociclib for 1 day in the presence/absence of the indicated growth inhibitor (MEKi, PD-0325901; AKTi$^{(allo)}$, MK2206; AKTi$^{(atp)}$, capivasertib). Western blot is representatives of 2 repeats.

(F) Quantification of γH2AX-positive foci and nuclear morphologies in indicated ARPE19 cells treated with DMSO or palbociclib for 7 days ± MK2206 (AKTi$^{(allo)}$) or capivasertib (AKTi$^{(atp)}$) and then analyzed 72 h after drug washout. Graphs show means - SD from three repeats.

experience even further DNA damage due to catastrophic chromosome segregation errors, promoting permanent exit from the cell cycle.[11,12,25,48] Future research will be important to determine how much these various routes to genotoxic stress contribute to cell cycle exit in cancer cells with different oncogenic mutations.

It is now crucial to validate these findings in animal models and patient samples because if oncogene-dependent cell overgrowth is important to drive DNA damage and cell cycle withdrawal *in vivo*, then this would have important clinical implications. Most importantly, it would rationalize effective combination therapies that converge to inhibit Cyclin D-CDK4/6 activity without affecting global mTOR-dependent translation. Interestingly, this is the predicted effect of hormone therapy in combination with CDK4/6 inhibitors, which is the current standard-of-care treatment in HR+/HER2− breast cancer.[3] This is

because steroid hormones such as estrogen and progesterone stimulate their receptors to translocate to the nucleus and enhance the transcription of Cyclin D.[49–52] Analogous synthetic lethal combinations have been proposed in clear cell renal cell carcinoma, where HIF2A stimulates Cyclin D transcription.[53] Furthermore, other combinations that act via similar principles have been identified, such as CK1ε inhibition, which represses SP1-mediated CDK6 transcription following CDK4/6 inhibition in breast cancer.[54] The ability of cancer cells to transcriptionally upregulate Cyclin D-CDK4/6 activity via various different routes suggests that similar effective combinations await discovery in other tumor types.

Many ongoing clinical trials are testing inhibitors of growth factor signaling pathways, such as PI3K, MEK, AKT, and mTOR, together with CDK4/6 inhibitors.[3,55] The fact that these combinations improve the G1 arrest has been extensively demonstrated in preclinical models; therefore, it is logical to assume that a similar sensitized G1 arrest may also be beneficial for treating patient tumors.[5,55,56] Nevertheless, the question of whether the resulting G1 arrest is cytostatic or cytotoxic is still likely to be important for the overall response, and this will depend on the mechanism(s) used to clear G1-arrested tumor cells *in vivo*. If this is via overgrowth-mediated cell cycle withdrawal, as we demonstrate, then the response will likely depend on the extent of overgrowth and how proteins scale, which will be defined by the oncogene(s) driving that growth and the particular drug combination used to arrest cells in G1. The concept is explained in Figures 7 and S7, which show that overgrowth and DNA damage depend on both inhibitor type and oncogenic context. Some combinations enhance oncogene-specific damage, whereas others reduce it. It is important to point out, however, that these drug combinations can lead to either senescence or apoptosis in preclinical models,[10] and it is debatable which endpoint is more clinically relevant, since some studies mainly report apoptosis,[57–59] whereas others predominantly show senescence.[60–63] It can be challenging to monitor senescence in clinical samples, but this is an important future goal, as discussed here.[64] At this stage, we would simply urge the monitoring of cell size and DNA damage in proliferating tumor cells, before and during treatment, to assess whether these properties change and, if so, whether the change is predictive of the overall response.

A major reason why drug combinations are needed to efficiently inhibit G1 progression is that cell growth itself acts to promote S-phase entry by producing Cyclin D and, thereby, elevating CDK4/6 activity. This is why mutations that enhance growth factor signaling have been associated with resistance to CDK4/6 inhibition in patients,[62,65,66] which begs the questions of how growth signals can drive both sensitivity and resistance. We propose that they can cause sensitivity to CDK4/6 inhibition if the G1 arrest is efficient, and overgrowth rises to intolerable levels, as we observe in different cell lines. However, growth signals can also drive resistance if the growth they produce is sufficient to bypass the G1 arrest and, crucially, if the resulting DNA damage and chromosome segregation errors experienced by large cells in S/M-phases are tolerable. In this case, the continued proliferation of these overgrown and damaged cells could facilitate the acquisition of resistant genotypes or karyotypes, such as the loss/mutation of p53, which allows CDK4/6 inhibitor-treated cells to proliferate despite extensive DNA damage (see Figures 4E–4H and S7F and Crozier et al.[11]), and is frequently associated with resistance in patients.[66,67] In fact, we previously observed that many p53-deficient cancer types continue to proliferate following CDK4/6 inhibition, albeit at a slower rate, and these cells gradually accrue DNA damage over time,[12] most probably because they proliferate while enlarged.

How then might we use this information to help tackle the crucial issue of drug resistance? We propose that if resistant cells *in vivo* become enlarged and damaged, then they should be vulnerable to secondary agents, such as chemotherapeutics that either enhance DNA damage or inhibit DNA damage repair. This may help explain the surprising finding that the CDK4/6 inhibitor trilaciclib improves the overall survival in triple-negative breast cancer when given prior to chemotherapy with the genotoxic combination of gemcitabine and carboplatin.[68] It could also help explain the well-established radio-sensitizing effects of CDK4/6 inhibition.[69] It will be important in future to screen for and test predicted vulnerabilities in enlarged CDK4/6-inhibitor-treated cells.

In summary, we demonstrate here that CDK4/6 inhibitors allow oncogenic signals to drive toxic cell overgrowth and cell cycle exit, which holds great promise for the long-term goal of achieving tumor selectivity with general cell cycle inhibitors. It is now crucial to validate these findings in animal models and patient samples because if these are also observed *in vivo*, then the ability of CDK4/6 inhibitors to switch pro-proliferative oncogenic signals into toxic anti-proliferative responses would represent a new paradigm for anti-cancer treatment. Tumors may be addicted to oncogenes for survival, but if this addiction could be turned into a liability by inhibiting the cell cycle, then oncogenes could prove to be cancer's Achilles heel.

Limitations of the study

This study demonstrates the importance of cell overgrowth for driving DNA damage and cell cycle exit in a range of cultured cell lines treated with CDK4/6 inhibitors. Future work will need to investigate whether these effects are also observed *in vivo*, in both animal models and clinical samples, following CDK4/6 inhibition with or without additional hormonal therapy. In these situations, it will also be important to examine cell size and DNA damage in drug-resistant cells that emerge during or following treatment. The situation *in vivo* is likely to be far more complex, especially since the clearance of senescence cells via the immune system will also be important for the overall response, and CDK4/6 inhibitors can affect immune clearance in many different ways.[9]

STAR★METHODS

Detailed methods are provided in the online version of this paper and include the following:

- KEY RESOURCES TABLE
- RESOURCE AVAILABILITY
  - Lead contact
  - Materials availability
  - Data and code availability

SUPPLEMENTAL INFORMATION

Supplemental information can be found online at https://doi.org/10.1016/j.molcel.2023.10.020.

ACKNOWLEDGMENTS

We thank the Dundee Imaging Facility, the Dundee FingerPrints Proteomics Facility, and Genetic Core Services for help with this work and Alexis Barr for the critical reading of this manuscript. We thank Edward Kaye (Dundee) for help with proteomics sample preparation. This work was supported by a Cancer Research UK Programme Foundation Award to A.T.S. (C47320/A21229), which also funds L.C. and R.F.; a Tenovus Scotland Studentship (that funded R.F.); a Medical Research Council (UK) Doctoral Training Program Studentship (that funded L.C.); a Ninewells Cancer Campaign studentship (that funds A.U.P.); a Sir Henry Dale Fellowship to T.L. (206211/A/17/Z and 218305/Z/19/Z); and a Wellcome Trust Investigator Award to A.T.S. (222494/Z/21/Z), which also funds J.M.V. B.H.P. is supported by the Breast Cancer Research Foundation and the Susan G. Komen Foundation.

AUTHOR CONTRIBUTIONS

A.T.S., R.F., and L.C. conceived the study, designed the experiments, and interpreted the data. R.F. and L.C. performed the majority of experiments with important contributions from A.U.P. J.M.V. processed the mass spec samples, and T.L. performed the mass spec data analysis. B.H.P. provided the MCF7 and MCF10A PI3K knockin cell lines. A.T.S. acquired funding, supervised the study, and wrote the manuscript, with help from R.F., L.C., and A.U.P.

DECLARATION OF INTERESTS

B.H.P. is a paid consultant for Jackson Labs, Jansen, Hologics, EQRx, Guardant Health, and Caris; a paid scientific advisory board member for Celcuity Inc.; and an unpaid consultant for Tempus Inc. Under separate licensing agreements between Horizon Discovery and the Johns Hopkins University, B.H.P. is entitled to a share of royalties received by the university on sales of products. The terms of this arrangement are being managed by the Johns Hopkins University in accordance with its conflict-of-interest policies.

INCLUSION AND DIVERSITY

We support inclusive, diverse, and equitable conduct of research.

Received: September 12, 2022
Revised: July 10, 2023
Accepted: October 17, 2023
Published: November 16, 2023

REFERENCES

1. Liu, J., Peng, Y., and Wei, W. (2022). Cell cycle on the crossroad of tumorigenesis and cancer therapy. Trends Cell Biol. *32*, 30–44. https://doi.org/10.1016/j.tcb.2021.07.001.
2. Suski, J.M., Braun, M., Strmiska, V., and Sicinski, P. (2021). Targeting cell-cycle machinery in cancer. Cancer Cell *39*, 759–778. https://doi.org/10.1016/j.ccell.2021.03.010.
3. Fassl, A., Geng, Y., and Sicinski, P. (2022). CDK4 and CDK6 kinases: from basic science to cancer therapy. Science *375*, eabc1495. https://doi.org/10.1126/science.abc1495.
4. Kent, L.N., and Leone, G. (2019). The broken cycle: E2F dysfunction in cancer. Nat. Rev. Cancer *19*, 326–338. https://doi.org/10.1038/s41568-019-0143-7.
5. Álvarez-Fernández, M., and Malumbres, M. (2020). Mechanisms of sensitivity and resistance to CDK4/6 inhibition. Cancer Cell *37*, 514–529. https://doi.org/10.1016/j.ccell.2020.03.010.
6. Choi, Y.J., Li, X., Hydbring, P., Sanda, T., Stefano, J., Christie, A.L., Signoretti, S., Look, A.T., Kung, A.L., von Boehmer, H., and Sicinski, P. (2012). The requirement for cyclin D function in tumor maintenance. Cancer Cell *22*, 438–451. https://doi.org/10.1016/j.ccr.2012.09.015.
7. Gong, X., Litchfield, L.M., Webster, Y., Chio, L.C., Wong, S.S., Stewart, T.R., Dowless, M., Dempsey, J., Zeng, Y., Torres, R., et al. (2017). Genomic aberrations that activate D-type cyclins are associated with enhanced sensitivity to the CDK4 and CDK6 inhibitor abemaciclib. Cancer Cell *32*, 761–776.e6. https://doi.org/10.1016/j.ccell.2017.11.006.
8. Klein, M.E., Kovatcheva, M., Davis, L.E., Tap, W.D., and Koff, A. (2018). CDK4/6 inhibitors: the mechanism of action may not be as simple as once thought. Cancer Cell *34*, 9–20. https://doi.org/10.1016/j.ccell.2018.03.023.
9. Zhang, S., Xu, Q., Sun, W., Zhou, J., and Zhou, J. (2023). Immunomodulatory effects of CDK4/6 inhibitors. Biochim. Biophys. Acta Rev. Cancer *1878*, 188912. https://doi.org/10.1016/j.bbcan.2023.188912.
10. Wagner, V., and Gil, J. (2020). Senescence as a therapeutically relevant response to CDK4/6 inhibitors. Oncogene *39*, 5165–5176. https://doi.org/10.1038/s41388-020-1354-9.
11. Crozier, L., Foy, R., Mouery, B.L., Whitaker, R.H., Corno, A., Spanos, C., Ly, T., Gowen Cook, J., and Saurin, A.T. (2022). CDK4/6 inhibitors induce replication stress to cause long-term cell cycle withdrawal. EMBO J. *41*, e108599. https://doi.org/10.15252/embj.2021108599.
12. Crozier, L., Foy, R., Adib, R., Badonyi, M., Kar, A., Holt, J.A., Wilson, R., Regnault, C., Whitfield, P., Marsh, J.A., et al. (2023). CDK4/6 inhibitor-mediated cell overgrowth triggers osmotic and replication stress to promote senescence. Mol. Cell *83*, 4062–4077. https://doi.org/10.1016/j.molcel.2023.10.016.
13. Ginzberg, M.B., Chang, N., D'Souza, H., Patel, N., Kafri, R., and Kirschner, M.W. (2018). Cell size sensing in animal cells coordinates anabolic growth rates and cell cycle progression to maintain cell size uniformity. eLife *7*, e26957. https://doi.org/10.7554/eLife.26957.
14. Zatulovskiy, E., Zhang, S., Berenson, D.F., Topacio, B.R., and Skotheim, J.M. (2020). Cell growth dilutes the cell cycle inhibitor Rb to trigger cell division. Science *369*, 466–471. https://doi.org/10.1126/science.aaz6213.
15. Neurohr, G.E., Terry, R.L., Lengefeld, J., Bonney, M., Brittingham, G.P., Moretto, F., Miettinen, T.P., Vaites, L.P., Soares, L.M., Paulo, J.A., et al. (2019). Excessive cell growth causes cytoplasm dilution and contributes to senescence. Cell *176*, 1083–1097.e18. https://doi.org/10.1016/j.cell.2019.01.018.
16. Lengefeld, J., Cheng, C.W., Maretich, P., Blair, M., Hagen, H., McReynolds, M.R., Sullivan, E., Majors, K., Roberts, C., Kang, J.H., et al. (2021). Cell size is a determinant of stem cell potential during aging. Sci. Adv. *7*, eabk0271. https://doi.org/10.1126/sciadv.abk0271.
17. Tan, C., Ginzberg, M.B., Webster, R., Iyengar, S., Liu, S., Papadopoli, D., Concannon, J., Wang, Y., Auld, D.S., Jenkins, J.L., et al. (2021). Cell size

homeostasis is maintained by CDK4-dependent activation of p38 MAPK. Dev. Cell *56*, 1756–1769.e7. https://doi.org/10.1016/j.devcel.2021.04.030.

18. Mallon, R., Feldberg, L.R., Lucas, J., Chaudhary, I., Dehnhardt, C., Santos, E.D., Chen, Z., dos Santos, O., Ayral-Kaloustian, S., Venkatesan, A., and Hollander, I. (2011). Antitumor efficacy of PKI-587, a highly potent dual PI3K/mTOR kinase inhibitor. Clin. Cancer Res. *17*, 3193–3203. https://doi.org/10.1158/1078-0432.CCR-10-1694.
19. Ruvinsky, I., Sharon, N., Lerer, T., Cohen, H., Stolovich-Rain, M., Nir, T., Dor, Y., Zisman, P., and Meyuhas, O. (2005). Ribosomal protein S6 phosphorylation is a determinant of cell size and glucose homeostasis. Genes Dev. *19*, 2199–2211. https://doi.org/10.1101/gad.351605.
20. Dufner, A., and Thomas, G. (1999). Ribosomal S6 kinase signaling and the control of translation. Exp. Cell Res. *253*, 100–109. https://doi.org/10.1006/excr.1999.4683.
21. Sakaue-Sawano, A., Kurokawa, H., Morimura, T., Hanyu, A., Hama, H., Osawa, H., Kashiwagi, S., Fukami, K., Miyata, T., Miyoshi, H., et al. (2008). Visualizing spatiotemporal dynamics of multicellular cell-cycle progression. Cell *132*, 487–498. https://doi.org/10.1016/j.cell.2007.12.033.
22. Leontieva, O.V., and Blagosklonny, M.V. (2013). CDK4/6-inhibiting drug substitutes for p21 and p16 in senescence: duration of cell cycle arrest and MTOR activity determine geroconversion. Cell Cycle *12*, 3063–3069. https://doi.org/10.4161/cc.26130.
23. Leontieva, O.V., Demidenko, Z.N., and Blagosklonny, M.V. (2013). MEK drives cyclin D1 hyperelevation during geroconversion. Cell Death Differ. *20*, 1241–1249. https://doi.org/10.1038/cdd.2013.86.
24. Maskey, R.S., Wang, F., Lehman, E., Wang, Y., Emmanuel, N., Zhong, W., Jin, G., Abraham, R.T., Arndt, K.T., Myers, J.S., and Mazurek, A. (2021). Sustained mTORC1 activity during palbociclib-induced growth arrest triggers senescence in ER+ breast cancer cells. Cell Cycle *20*, 65–80. https://doi.org/10.1080/15384101.2020.1859195.
25. Manohar, S., Estrada, M.E., Uliana, F., and Neurohr, G.E. (2023). Genome homeostasis defects drive enlarged cells into senescence. Molecular Cell *83*, 4032–4046. https://doi.org/10.1016/j.molcel.2023.10.018.
26. Mendonsa, A.M., Na, T.Y., and Gumbiner, B.M. (2018). E-cadherin in contact inhibition and cancer. Oncogene *37*, 4769–4780. https://doi.org/10.1038/s41388-018-0304-2.
27. Hirai, H., Sootome, H., Nakatsuru, Y., Miyama, K., Taguchi, S., Tsujioka, K., Ueno, Y., Hatch, H., Majumder, P.K., Pan, B.S., and Kotani, H. (2010). MK-2206, an allosteric Akt inhibitor, enhances antitumor efficacy by standard chemotherapeutic agents or molecular targeted drugs in vitro and in vivo. Mol. Cancer Ther. *9*, 1956–1967. https://doi.org/10.1158/1535-7163.MCT-09-1012.
28. Beaver, J.A., Gustin, J.P., Yi, K.H., Rajpurohit, A., Thomas, M., Gilbert, S.F., Rosen, D.M., Ho Park, B., and Lauring, J. (2013). PIK3CA and AKT1 mutations have distinct effects on sensitivity to targeted pathway inhibitors in an isogenic luminal breast cancer model system. Clin. Cancer Res. *19*, 5413–5422. https://doi.org/10.1158/1078-0432.CCR-13-0884.
29. Libouban, M.A.A., de Roos, J.A.D.M., Uitdehaag, J.C.M., Willemsen-Seegers, N., Mainardi, S., Dylus, J., de Man, J., Tops, B., Meijerink, J.P.P., Storchová, Z., et al. (2017). Stable aneuploid tumors cells are more sensitive to TTK inhibition than chromosomally unstable cell lines. Oncotarget *8*, 38309–38325. https://doi.org/10.18632/oncotarget.16213.
30. Di Nicolantonio, F., Arena, S., Gallicchio, M., Zecchin, D., Martini, M., Flonta, S.E., Stella, G.M., Lamba, S., Cancelliere, C., Russo, M., et al. (2008). Replacement of normal with mutant alleles in the genome of normal human cells unveils mutation-specific drug responses. Proc. Natl. Acad. Sci. USA *105*, 20864–20869. https://doi.org/10.1073/pnas.0808757105.
31. Gustin, J.P., Karakas, B., Weiss, M.B., Abukhdeir, A.M., Lauring, J., Garay, J.P., Cosgrove, D., Tamaki, A., Konishi, H., Konishi, Y., et al. (2009). Knockin of mutant PIK3CA activates multiple oncogenic pathways. Proc. Natl. Acad. Sci. USA *106*, 2835–2840. https://doi.org/10.1073/pnas.0813351106.
32. Molina-Arcas, M., Hancock, D.C., Sheridan, C., Kumar, M.S., and Downward, J. (2013). Coordinate direct input of both KRAS and IGF1 receptor to activation of PI3 kinase in KRAS-mutant lung cancer. Cancer Discov. *3*, 548–563. https://doi.org/10.1158/2159-8290.CD-12-0446.
33. Salic, A., and Mitchison, T.J. (2008). A chemical method for fast and sensitive detection of DNA synthesis *in vivo*. Proc. Natl. Acad. Sci. 105. https://doi.org/10.1073/pnas.0712168105.
34. Freeman-Cook, K., Hoffman, R.L., Miller, N., Almaden, J., Chionis, J., Zhang, Q., Eisele, K., Liu, C., Zhang, C., Huser, N., et al. (2021). Expanding control of the tumor cell cycle with a CDK2/4/6 inhibitor. Cancer Cell *39*, 1404–1421.e11. https://doi.org/10.1016/j.ccell.2021.08.009.
35. Freeman-Cook, K.D., Hoffman, R.L., Behenna, D.C., Boras, B., Carelli, J., Diehl, W., Ferre, R.A., He, Y.A., Hui, A., Huang, B., et al. (2021). Discovery of PF-06873600, a CDK2/4/6 inhibitor for the treatment of cancer. J. Med. Chem. *64*, 9056–9077. https://doi.org/10.1021/acs.jmedchem.1c00159.
36. Schmoller, K.M., Turner, J.J., Kõivomägi, M., and Skotheim, J.M. (2015). Dilution of the cell cycle inhibitor Whi5 controls budding-yeast cell size. Nature *526*, 268–272. https://doi.org/10.1038/nature14908.
37. D'Ario, M., Tavares, R., Schiessl, K., Desvoyes, B., Gutierrez, C., Howard, M., and Sablowski, R. (2021). Cell size controlled in plants using DNA content as an internal scale. Science *372*, 1176–1181. https://doi.org/10.1126/science.abb4348.
38. Øvrebø, J.I., Ma, Y., and Edgar, B.A. (2022). Cell growth and the cell cycle: new insights about persistent questions. Bioessays *44*, e2200150. https://doi.org/10.1002/bies.202200150.
39. Xie, S., Swaffer, M., and Skotheim, J.M. (2022). Eukaryotic cell size control and its relation to biosynthesis and senescence. Annu. Rev. Cell Dev. Biol. *38*, 291–319. https://doi.org/10.1146/annurev-cellbio-120219-040142.
40. Arora, M., Moser, J., Hoffman, T.E., Watts, L.P., Min, M., Musteanu, M., Rong, Y., III, C.R., Nangia, V., Schneider, J., et al. (2023). Rapid adaptation to CDK2 inhibition exposes intrinsic cell-cycle plasticity. Cell *186*, 2628–2643.e21. https://doi.org/10.1016/j.cell.2023.05.013.
41. Kotsantis, P., Petermann, E., and Boulton, S.J. (2018). Mechanisms of oncogene-induced replication stress: jigsaw falling into place. Cancer Discov. *8*, 537–555. https://doi.org/10.1158/2159-8290.CD-17-1461.
42. Herman, J.A., Romain, R.R., Hoellerbauer, P., Shirnekhi, H.K., King, D.C., DeLuca, K.F., Osborne Nishimura, E., Paddison, P.J., and DeLuca, J.G. (2022). Hyper-active RAS/MAPK introduces cancer-specific mitotic vulnerabilities. Proc. Natl. Acad. Sci. USA *119*, e2208255119. https://doi.org/10.1073/pnas.2208255119.
43. Rehan, M., Beg, M.A., Parveen, S., Damanhouri, G.A., and Zaher, G.F. (2014). Computational insights into the inhibitory mechanism of human AKT1 by an orally active inhibitor, MK-2206. PLOS One *9*, e109705. https://doi.org/10.1371/journal.pone.0109705.
44. Wilson, G.A., Sava, G., Vuina, K., Huard, C., Meneguello, L., Coulombe-Huntington, J., Bertomeu, T., Maizels, R.J., Lauring, J., Tyers, M., et al. (2023). Active growth signaling promotes senescence and cancer cell sensitivity to CDK7 inhibition. Molecular Cell *83*, 4078–4092. https://doi.org/10.1016/j.molcel.2023.10.017.
45. Blagosklonny, M.V. (2003). Cell senescence and hypermitogenic arrest. EMBO Rep. *4*, 358–362. https://doi.org/10.1038/sj.embor.embor806.
46. Blagosklonny, M.V. (2022). Cell senescence, rapamycin and hyperfunction theory of aging. Cell Cycle *21*, 1456–1467. https://doi.org/10.1080/15384101.2022.2054636.
47. Lanz, M.C., Zatulovskiy, E., Swaffer, M.P., Zhang, L., Ilerten, I., Zhang, S., You, D.S., Marinov, G., McAlpine, P., Elias, J.E., and Skotheim, J.M. (2022). Increasing cell size remodels the proteome and promotes senescence. Mol. Cell *82*, 3255–3269.e8. https://doi.org/10.1016/j.molcel.2022.07.017.
48. Wang, B., Varela-Eirin, M., Brandenburg, S.M., Hernandez-Segura, A., van Vliet, T., Jongbloed, E.M., Wilting, S.M., Ohtani, N., Jager, A., and Demaria, M. (2022). Pharmacological CDK4/6 inhibition reveals a

p53-dependent senescent state with restricted toxicity. EMBO J. *41*, e108946. https://doi.org/10.15252/embj.2021108946.

49. Sabbah, M., Courilleau, D., Mester, J., and Redeuilh, G. (1999). Estrogen induction of the cyclin D1 promoter: involvement of a cAMP response-like element. Proc. Natl. Acad. Sci. USA *96*, 11217–11222. https://doi.org/10.1073/pnas.96.20.11217.

50. Prall, O.W., Sarcevic, B., Musgrove, E.A., Watts, C.K., and Sutherland, R.L. (1997). Estrogen-induced activation of Cdk4 and Cdk2 during G1-S phase progression is accompanied by increased cyclin D1 expression and decreased cyclin-dependent kinase inhibitor association with cyclin E-Cdk2. J. Biol. Chem. *272*, 10882–10894. https://doi.org/10.1074/jbc.272.16.10882.

51. Giulianelli, S., Vaque, J.P., Soldati, R., Wargon, V., Vanzulli, S.I., Martins, R., Zeitlin, E., Molinolo, A.A., Helguero, L.A., Lamb, C.A., et al. (2012). Estrogen receptor alpha mediates progestin-induced mammary tumor growth by interacting with progesterone receptors at the Cyclin D1/MYC promoters. Cancer Res *72*, 2416–2427. https://doi.org/10.1158/0008-5472.CAN-11-3290.

52. Cicatiello, L., Addeo, R., Sasso, A., Altucci, L., Petrizzi, V.B., Borgo, R., Cancemi, M., Caporali, S., Caristi, S., Scafoglio, C., et al. (2004). Estrogens and progesterone promote persistent *CCND1* gene activation during G_1 by inducing transcriptional derepression via c-*Jun*/c-*Fos*/estrogen receptor (progesterone receptor) complex assembly to a distal regulatory element and recruitment of Cyclin D1 to its own gene promoter. Molecular and Cellular Biology *24*, 7260–7274. https://doi.org/10.1128/MCB.24.16.7260-7274.2004.

53. Nicholson, H.E., Tariq, Z., Housden, B.E., Jennings, R.B., Stransky, L.A., Perrimon, N., Signoretti, S., and Kaelin, W.G., Jr. (2019). HIF-independent synthetic lethality between CDK4/6 inhibition and VHL loss across species. Sci. Signal. *12*, eaay0482. https://doi.org/10.1126/scisignal.aay0482.

54. Dang, F., Nie, L., Zhou, J., Shimizu, K., Chu, C., Wu, Z., Fassl, A., Ke, S., Wang, Y., Zhang, J., et al. (2021). Inhibition of CK1ε potentiates the therapeutic efficacy of CDK4/6 inhibitor in breast cancer. Nat. Commun. *12*, 5386. https://doi.org/10.1038/s41467-021-25700-6.

55. Malumbres, M. (2019). CDK4/6 inhibitors: what is the best cocktail? Clin. Cancer Res. *25*, 6–8. https://doi.org/10.1158/1078-0432.CCR-18-2177.

56. Watt, A.C., and Goel, S. (2022). Cellular mechanisms underlying response and resistance to CDK4/6 inhibitors in the treatment of hormone receptor-positive breast cancer. Breast Cancer Res. *24*, 17. https://doi.org/10.1186/s13058-022-01510-6.

57. Jansen, V.M., Bhola, N.E., Bauer, J.A., Formisano, L., Lee, K.M., Hutchinson, K.E., Witkiewicz, A.K., Moore, P.D., Estrada, M.V., Sánchez, V., et al. (2017). Kinome-wide RNA interference screen reveals a role for PDK1 in acquired resistance to CDK4/6 inhibition in ER-positive breast cancer. Cancer Res. *77*, 2488–2499. https://doi.org/10.1158/0008-5472.CAN-16-2653.

58. Zhao, M., Scott, S., Evans, K.W., Yuca, E., Saridogan, T., Zheng, X., Wang, H., Korkut, A., Cruz Pico, C.X., Demirhan, M., et al. (2021). Combining neratinib with CDK4/6, mTOR, and MEK inhibitors in models of HER2-positive cancer. Clin. Cancer Res. *27*, 1681–1694. https://doi.org/10.1158/1078-0432.CCR-20-3017.

59. Herrera-Abreu, M.T., Palafox, M., Asghar, U., Rivas, M.A., Cutts, R.J., Garcia-Murillas, I., Pearson, A., Guzman, M., Rodriguez, O., Grueso, J., et al. (2016). Early adaptation and acquired resistance to CDK4/6 inhibition in estrogen receptor-positive breast cancer. Cancer Res. *76*, 2301–2313. https://doi.org/10.1158/0008-5472.CAN-15-0728.

60. Michaloglou, C., Crafter, C., Siersbaek, R., Delpuech, O., Curwen, J.O., Carnevalli, L.S., Staniszewska, A.D., Polanska, U.M., Cheraghchi-Bashi, A., Lawson, M., et al. (2018). Combined inhibition of mTOR and CDK4/6 is required for optimal blockade of E2F function and long-term growth inhibition in estrogen receptor-positive breast cancer. Mol. Cancer Ther. *17*, 908–920. https://doi.org/10.1158/1535-7163.MCT-17-0537.

61. Goel, S., Wang, Q., Watt, A.C., Tolaney, S.M., Dillon, D.A., Li, W., Ramm, S., Palmer, A.C., Yuzugullu, H., Varadan, V., et al. (2016). Overcoming therapeutic resistance in HER2-positive breast cancers with CDK4/6 inhibitors. Cancer Cell *29*, 255–269. https://doi.org/10.1016/j.ccell.2016.02.006.

62. Formisano, L., Lu, Y., Servetto, A., Hanker, A.B., Jansen, V.M., Bauer, J.A., Sudhan, D.R., Guerrero-Zotano, A.L., Croessmann, S., Guo, Y., et al. (2019). Aberrant FGFR signaling mediates resistance to CDK4/6 inhibitors in ER+ breast cancer. Nat. Commun. *10*, 1373. https://doi.org/10.1038/s41467-019-09068-2.

63. Vora, S.R., Juric, D., Kim, N., Mino-Kenudson, M., Huynh, T., Costa, C., Lockerman, E.L., Pollack, S.F., Liu, M., Li, X., et al. (2014). CDK 4/6 inhibitors sensitize PIK3CA mutant breast cancer to PI3K inhibitors. Cancer Cell *26*, 136–149. https://doi.org/10.1016/j.ccr.2014.05.020.

64. Witkiewicz, A.K., Kumarasamy, V., Sanidas, I., and Knudsen, E.S. (2022). Cancer cell cycle dystopia: heterogeneity, plasticity, and therapy. Trends Cancer *8*, 711–725. https://doi.org/10.1016/j.trecan.2022.04.006.

65. Costa, C., Wang, Y., Ly, A., Hosono, Y., Murchie, E., Walmsley, C.S., Huynh, T., Healy, C., Peterson, R., Yanase, S., et al. (2020). PTEN loss mediates clinical cross-resistance to CDK4/6 and PI3Kα inhibitors in breast cancer. Cancer Discov. *10*, 72–85. https://doi.org/10.1158/2159-8290.CD-18-0830.

66. Wander, S.A., Cohen, O., Gong, X., Johnson, G.N., Buendia-Buendia, J.E., Lloyd, M.R., Kim, D., Luo, F., Mao, P., Helvie, K., et al. (2020). The genomic landscape of intrinsic and acquired resistance to cyclin-dependent kinase 4/6 inhibitors in patients with hormone receptor-positive metastatic breast cancer. Cancer Discov. *10*, 1174–1193. https://doi.org/10.1158/2159-8290.CD-19-1390.

67. Patnaik, A., Rosen, L.S., Tolaney, S.M., Tolcher, A.W., Goldman, J.W., Gandhi, L., Papadopoulos, K.P., Beeram, M., Rasco, D.W., Hilton, J.F., et al. (2016). Efficacy and safety of abemaciclib, an inhibitor of CDK4 and CDK6, for patients with breast cancer, non-small cell lung cancer, and other solid tumors. Cancer Discov. *6*, 740–753. https://doi.org/10.1158/2159-8290.CD-16-0095.

68. Tan, A.R., Wright, G.S., Thummala, A.R., Danso, M.A., Popovic, L., Pluard, T.J., Han, H.S., Vojnović, Ž., Vasev, N., Ma, L., et al. (2022). Trilaciclib prior to chemotherapy in patients with metastatic triple-negative breast cancer: final efficacy and subgroup analysis from a randomized Phase II study. Clin. Cancer Res. *28*, 629–636. https://doi.org/10.1158/1078-0432.CCR-21-2272.

69. Yang, Y., Luo, J., Chen, X., Yang, Z., Mei, X., Ma, J., Zhang, Z., Guo, X., and Yu, X. (2020). CDK4/6 inhibitors: a novel strategy for tumor radiosensitization. J. Exp. Clin. Cancer Res. *39*, 188. https://doi.org/10.1186/s13046-020-01693-w.

70. Perez-Riverol, Y., Bai, J., Bandla, C., Garcia-Seisdedos, D., Hewapathirana, S., Kamatchinathan, S., Kundu, D.J., Prakash, A., Frericks-Zipper, A., Eisenacher, M., et al. (2022). The PRIDE database resources in 2022: a hub for mass spectrometry-based proteomics evidences. Nucleic Acids Research *50*, D543–D552. https://doi.org/10.1093/nar/gkab1038.

71. Krenning, L., Feringa, F.M., Shaltiel, I.A., van den Berg, J., and Medema, R.H. (2014). Transient activation of p53 in G2 phase is sufficient to induce senescence. Mol. Cell *55*, 59–72. https://doi.org/10.1016/j.molcel.2014.05.007.

72. McKinley, K.L., and Cheeseman, I.M. (2017). Large-scale analysis of CRISPR/Cas9 cell-cycle knockouts reveals the diversity of p53-dependent responses to cell-cycle defects. Dev. Cell *40*, 405–420.e2. https://doi.org/10.1016/j.devcel.2017.01.012.

73. Schindelin, J., Arganda-Carreras, I., Frise, E., Kaynig, V., Longair, M., Pietzsch, T., Preibisch, S., Rueden, C., Saalfeld, S., Schmid, B., et al. (2012). Fiji: an open-source platform for biological-image analysis. Nat. Method. *9*, 676–682. https://doi.org/10.1038/nmeth.2019.

74. Postma, M., and Goedhart, J. (2019). PlotsOfData-A web app for visualizing data together with their summaries. PLoS Biol. *17*, e3000202. https://doi.org/10.1371/journal.pbio.3000202.

75. Edelstein, A., Amodaj, N., Hoover, K., Vale, R., and Stuurman, N. (2010). Computer control of microscopes using μManager. Curr. Protoc. Mol. Biol. *92*, 14.20.1–14.20.17. https://doi.org/10.1002/0471142727.mb1420s92.

76. Kohn, A.D., Takeuchi, F., and Roth, R.A. (1996). Akt, a pleckstrin homology domain containing kinase, is activated primarily by phosphorylation. J. Biol. Chem. *271*, 21920–21926. https://doi.org/10.1074/jbc.271.36.21920.

77. Brunet, A., Pagès, G., and Pouysségur, J. (1994). Constitutively active mutants of MAP kinase kinase (MEK1) induce growth factor-relaxation and oncogenicity when expressed in fibroblasts. Oncogene *9*, 3379–3387.

78. Serrano, M., Lin, A.W., McCurrach, M.E., Beach, D., and Lowe, S.W. (1997). Oncogenic ras provokes premature cell senescence associated with accumulation of p53 and p16INK4a. Cell *88*, 593–602. https://doi.org/10.1016/s0092-8674(00)81902-9.

79. Munoz, I.M., Szyniarowski, P., Toth, R., Rouse, J., and Lachaud, C. (2014). Improved genome editing in human cell lines using the CRISPR method. Plos One. https://doi.org/10.1371/journal.pone.0109752.

80. Reyes, L., Sanchez-Garcia, M.A., Morrison, T., Howden, A.J.M., Watts, E.R., Arienti, S., Sadiku, P., Coelho, P., Mirchandani, A.S., Zhang, A., et al. (2021). A type I IFN, prothrombotic hyperinflammatory neutrophil signature is distinct for COVID-19 ARDS–. Wellcome Open Res. *6*, 38. https://doi.org/10.12688/wellcomeopenres.16584.2.

81. Wiśniewski, J.R., Hein, M.Y., Cox, J., and Mann, M. (2014). A "proteomic ruler" for protein copy number and concentration estimation without spike-in standards. Mol. Cell. Proteomics *13*, 3497–3506. https://doi.org/10.1074/mcp.M113.037309.

82. Jovanovic, M., Rooney, M.S., Mertins, P., Przybylski, D., Chevrier, N., Satija, R., Rodriguez, E.H., Fields, A.P., Schwartz, S., Raychowdhury, R., et al. (2015). Immunogenetics. Dynamic profiling of the protein life cycle in response to pathogens. Science *347*, 1259038. https://doi.org/10.1126/science.1259038.

STAR★METHODS

KEY RESOURCES TABLE

REAGENT or RESOURCE	SOURCE	IDENTIFIER
Antibodies		
Mouse anti-phospho-Histone H2A.X, clone JBW301	Sigma	Cat# 05-636, RRID:AB_309864
Mouse anti-tubulin (clone B-5-1-2)	Sigma	Cat# T5168-2ML, RRID: AB_477579
Rabbit anti-p21 Waf1/Cip1 (12D1)	Cell Signaling Technology	Cat# 2947, RRID: AB_823586
Rabbit anti-phospho-Rb (Ser807/811) (D20B12)	Cell Signaling Technology	Cat# 8516S, RRID: AB_11178658
Rabbit anti-phospho-S6 ribosomal protein (Ser235/236)	Cell Signaling Technology	Cat# 4858, RRID: AB_916156
Rabbit anti-actin	Sigma	Cat# A2066, RRID: AB_476693
Rabbit anti-phospho-AKT (Ser473) (D9E)	Cell Signaling Technology	Cat# 4060S, RRID: AB_2315049
Rabbit anti-AKT	Cell Signaling Technology	Cat# 9272, RRID: AB_329827
Rabbit anti-ERK1/2	Upstate	Cat# 06-182, RRID:AB_310068
Mouse anti-phospho-p44/42 MAPK (ERK1/2) (Thr202/Thr204) (E10)	Cell Signaling Technology	Cat# 9106S, RRID: AB_331768
Mouse anti-p53 (DO-1)	Santa Cruz	Cat# sc-126, RRID: AB_628082
Goat anti- Mouse Alexa Fluor 488	Thermo Fisher	Cat# A-11029, RRID: AB_2534088
Goat anti- Rabbit Alexa Fluor 568	Thermo Fisher	Cat# A-11036, RRID: AB_10563566
IRDye 800CW Goat anti-mouse IgG	LI-COR	Cat# 926-32210, RRID: AB_621842
IRDye 800CW Donkey anti-rabbit IgG	LI-COR	Cat# 926-32213, RRID: AB_621848
IRDye 680RD Goat anti-mouse IgG	LI-COR	Cat# 925-68070, RRID: AB_2651128
IRDye 680RD Goat anti-rabbit IgG	LI-COR	Cat# 925-68071, RRID: AB_2721181
Chemicals, peptides, and recombinant proteins		
Palbociclib	MedChemExpress	Cat# HY-50767
PF-05212384 (Gedatolisib)	Sigma	Cat# PZ0281
PD0325901 (Mirdamentinib)	Selleckchem	Cat# S1036
MK-2206 ($AKTi^{allo}$)	MedChemExpress	Cat# HY-108232
Nutlin-3a	Sigma	Cat# SML0580
PF-06873600 (CDK2/4/6i)	Cayman Chemical	Cat# 35502
(Z)-4-Hydroxytamoxifen	Sigma	Cat# H7904-5MG
Capivasertib ($AKTi^{ATP}$)	Insight Biotech	Cat# HY-15431-1ML
S-Trityl-L-cysteine	Sigma	Cat# 164739
DAPI (4',6-Diamidino-2-Phenylindole, Dihydrochloride)	Thermo Fisher Scientific	Cat# D1306
Penicillin/Streptomycin	Thermo Fisher Scientific, Gibco	Cat# 15070-063
Hydrocortisone	Sigma	Cat# H0888
Cholera Toxin	Sigma	Cat# C8052
EGF	Sigma	Cat# E9644
Insulin	Sigma	Cat# I9278
Etoposide	MedChemExpress	Cat# HY-13629
Critical commercial assays		
Base Click EdU Staining kit	Sigma	Cat# BCK-EdU488
Deposited data		
Mass spec proteomics data	PRIDE[70]	PRIDE: PXD043792

(*Continued on next page*)

Continued

REAGENT or RESOURCE	SOURCE	IDENTIFIER
Experimental models: Cell lines		
hTERT-RPE1	ATCC	Cat# CRL-4000; RRID: CVCL_4388
hTERT-RPE1 p53 KO	Crozier et al.[11,12]	N/A
RPE1-FUCCI	Krenning et al.[71]	N/A
MCF7	ATCC	Cat# HTB-22; RRID: CVCL_0031
T47D	ATCC	Cat# HTB-133, RRID:CVCL_0553
MCF7 parental (PI3KA-E545K)	Beaver et al.[28]	N/A
MCF7 corrected (PI3KA-WT-K545E)	Beaver et al.[28]	N/A
MCF10A parental	ATCC	Cat# CRL-10317, RRID: CVCL_0598
MCF10A PI3K-E545K	Gustin et al.[31]	N/A
MCF10A PI3K-H1047R	Gustin et al.[31]	N/A
MCF10A -ER-hRAS-G12V	Molina-Arcas et al.[32]	N/A
MCF10A parental p53 KO	This study	N/A
MCF10A PI3K-E545K p53 KO	This study	N/A
MCF10A PI3K-H1047R p53 KO	This study	N/A
MCF10A -ER-hRAS-G12V p53 KO	This study	N/A
MCF10A parental p21 KO	This study	N/A
MCF10A PI3K-E545K p21 KO	This study	N/A
MCF10A PI3K-H1047R p21 KO	This study	N/A
MCF10A -ER-hRAS-G12V p21 KO	This study	N/A
ARPE19	Herman et al.[42]	N/A
ARPE19 mut-p53	Herman et al.[42]	N/A
ARPE19 Tp53 AKT^{Myr}	Herman et al.[42]	N/A
ARPE19 Tp53 MEK^{DD}	Herman et al.[42]	N/A
ARPE19 Tp53 $hRAS^{V12}$	Herman et al.[42]	N/A
Oligonucleotides		
Targeting sequence for p53 KO gRNA: ACCAGCAGCTCCTACACCGGCGG	Crozier et al.[11,12]	N/A
Targeting sequence for p21 KO gRNA: CCGCGACTGTGATGCGCTAATGG	McKinley et al.[72]	N/A
Recombinant DNA		
pcDNA5-Cas9	MRCPPU reagents DU48261	N/A
Software and algorithms		
GraphPad Prism 6	GraphPad Software	N/A
Fiji	Schindelin et al.[73]	https://imagej.net/Fiji
Flowing software	Turku Bioscience	https://bioscience.fi/services/cell-imaging/flowing-software/
Holomonitor software	Holomonitor App Suite v3.4.0.158	N/A
Plotsofdata	Postma and Goedhart[74]	https://huygens.science.uva.nl/PlotsOfData/
Micro-Manager	Edelstein et al.[75]	https://micro-manager.org/

RESOURCE AVAILABILITY

Lead contact

Further information and requests for resources and reagents should be directed to and will be fulfilled by the lead contact, Adrian Saurin (a.saurin@dundee.ac.uk).

Materials availability

Cell lines generated in this study can be provided by the lead contact upon request.

Data and code availability

- The mass spectrometry proteomics data have been deposited to the ProteomeXchange Consortium via the PRIDE[70] partner repository with the dataset identifier PXD043792 Accession numbers are listed in the key resources table.
- This paper does not report original code.
- Any additional information required to reanalyze the data reported in this paper is available from the lead contact upon request.

EXPERIMENTAL MODEL AND STUDY PARTICIPANT DETAILS

hTERT-RPE1 (RPE1 sex=male) cells were purchased from ATCC and the RPE1-FUCCI were published previously.[71] The human ER+/HER2- breast cancer lines, MCF7 and T47D, were purchased from ATCC (sex=female). The MCF7 parental (PI3KA-E545K) and corrected (PI3KA-WT) cell lines are described in Beaver et al.[28] (sex=female). The MCF10A PI3K-E545K and H1047R knock-in lines are described in Gustin et al.[31] and the tamoxifen-inducible MCF10-ER- $hRAS^{V12}$ lines is described in Molina-Arcas et al.[32] (sex=female). Tamoxifen was added at 250 nM for all experiments with the MCF10A- $hRAS^{V12}$ line. The ARPE19 parental and oncogenic lines were published previously[42](sex=male). We specifically chose these cells because they had previously been transduced with TERT, $mTP53^{DD}$, CCDN1 and $CDK4^{R24C}$, which promotes CyclinD1/CDK4-dependent G1 progression to inhibit oncogene-induced senescence.[42] Therefore, we hypothesised this would lead to strong CDK4/6 dependence. The AKT^{myr} contains a 14aa myristylation sequence from src in place of the PH domain at the N-terminus of AKT.[76] MEK^{DD} is MEK1 from Chinese hamster lung fibroblasts cells in which S218 and S222 have phosphomimetic aspartate substitutions, resulting in 5-fold higher activity than following serum stimulation.[77] $hRAS^{V12}$ is a constitutively active hRAS mutant that has been validated previously.[78] All cells were authenticated by STR profiling (Eurofins) and screened for mycoplasma every 1–2 months.

RPE, MCF7 and T47D cells were cultured at 37°C with 5% CO_2 in DMEM (Thermo Fisher Scientific, Gibco 41966029) supplemented with 9% FBS (Thermo Fisher Scientific, Gibco 10270106) and 50 μg/ml penicillin/streptomycin (Sigma, P4458). ARPE19 cells were cultured at 37°C with 5% CO^2 in F12/DMEM (Thermo Fischer Scientific, Gibco, 11320033) supplemented with 9% FBS (Thermo Fisher Scientific, Gibco 10270106) and 50 μg/ml penicillin/streptomycin (Sigma, P4458). MCF10A cells were cultured at 37°C with 5% CO^2 in F12/DMEM (Thermo Fischer Scientific, Gibco, 11320033) and supplemented with 5% horse serum (Thermo Fischer Scientific, Gibco 16050122), 20ng/mg EGF (Sigma, E9644), 0.5ug/ml hydrocortisone (Sigma, H088), 100ng/ml cholera toxin (Sigma, C8052), 10ug/ml insulin (Sigma, I9278) and 50ug/ml penicillin/streptomycin (Sigma, P4458).

Drug concentrations

The following drugs were used at the indicated concentration: Palbociclib (CDK4/6i: PD-0332991: 1.25μM in RPE1/RPE1-FUCCI/ARPE19, 1μM in MCF7/T47D/MCF10A), EdU (used at 1μM), PF-05212384 (PF05: 30nM in RPE1/RPE1-FUCCI/ARPE19/MCF10A, 7.5nM in MCF7/T47D, unless stated otherwise), PD-0325901 (MEKi: Mirdametinib: 1.25μM), MK2206 ($AKTi^{(allo)}$: 1μM), nutlin-3a (5μM), PF-06873600 (CDK2/4/6i: 1μM), (Z)-4-Hydroxytamoxifen (250nM), capivasertib ($AKTi^{(atp)}$: 1μM), S-Trityl-L-cysteine (STLC: 10μM), etoposide (50μM).

METHOD DETAILS

Generation of knockout cell lines

p53 or p21 knockout MCF10A cell lines were generated by CRISPR/Cas9 using a gRNA which was made by site directed mutagenesis as described previously (Munoz et al.[79]). The gRNAs targeted exon 4 of TP53 (ACCAGCAGCTCCTACACCGGCGG) or exon 2 of CDKN1A (p21) (CCGCGACTGTGATGCGCTAATGG). The cells were transfected with the gRNA vector along with a pcDNA5-Cas9 vector in a 3:1 ratio (gRNA:Cas9) using Fugene HD (Promega, E2311). The cells were selected in 5μM Nutlin-3A until no visible cells remained on the control non-transfected plates (approximately 3 weeks).

Cell density

To prevent cell–cell contact from inhibiting exit from G1, it was crucial to plate cells at low density for all experiments, except those plated at high confluence shown in Figure 2 (in this case cells were plated at 100% confluence). This is especially true for RPE1 cells that arrest the cell cycle upon contact inhibition. Therefore, cells were plated at a maximum density of 8,000 cells per cm^2 immediately prior to the arrest with CDK4/6 inhibitors. For high confluence FUCCI experiments, the cells were re-plated into low confluence immediately before palbociclib washout to ensure re-entry into the cell cycle.

Cell volume measurements

For volume measurement, cells were plated in 6-well plates with palbociclib -/+ other treatments for 1-4 days. Washed and trypsinised cells were analysed on an NC-3000 Nucleocounter to quantify diameter using DAPI and Acridine orange. The histograms containing information of cell diameter was imported to Flowing Software version 5.2.1 and the appropriate gates were added to include the main peak of the histogram. Cell volume was then calculated as $\frac{4}{3}\pi r^3$.

Determining protein and RNA concentration

For protein and RNA concentration measurements, cells were plated in 10cm dishes with 1μM palbociclib for 1-7 days, after which cells were harvested and protein concentration calculated with a detergent compatible (DC) assay (BioRad), or RNA concentration determined using a Trizol-based method (Thermo Fisher Scientific, Invitrogen 15596018).

FUCCI experiments

For all FUCCI experiments, STLC was added to prevent progression past the first mitosis. The single-cell FUCCI profiles were generated manually by analysing RPE1-FUCCI movies. A total of 50 red cells were randomly selected and marked at the beginning of the movie. The time points in which the FUCCI cells change colour was recorded to determine the time spent in each phase of the first cell cycle following release from CDK4/6 inhibition. RPE-FUCCI cells were always imaged with the same illumination settings and all images were placed on the same scale prior to analysis to ensure that the red/yellow/green cut-offs were reproducibly calculated between experiments. Mitotic entry was timed based on the visualization of typical mitotic cell rounding and loss of nuclear mAG-geminin signal.

Immunofluorescence

Cells were plated at low density on High Precision 1.5H 12-mm coverslips (Marienfeld) and fixed for 10 min with 4% paraformaldehyde dissolved in PBS. Once fixed, coverslips were washed three times in PBS and then blocked in 3% BSA dissolved in PBS with 0.5% Triton X-100 for 30 min. Coverslips were then incubated with primary antibodies at 4°C overnight, prior to washing with PBS and incubation with secondary antibodies and DAPI (1 μg/ml) for 2–4 h at room temperature. After further washing, coverslips were mounted onto slides with ProLong Gold Antifade (Thermo Fisher Scientific, P10144). Coverslips were imaged on either a Zeiss Axio Observer using a Plan-apochromat 20×/0.8 M27 Air objective or a Deltavision with a 100×/1.40 NA U Plan S Apochromat objective. The primary antibodies used were as follows: mouse anti-phospho-Histone H2A.X (Ser139; clone JBW301; Sigma, 05-636; 1/1,000), mouse anti-tubulin (clone B-5-1-2, Sigma, T5168-.2ML; 1/5000), and rabbit p21 Waf1/Cip1 (clone 12D1, Cell Signaling Technology, #2947, 1:1000), rabbit phospho-Rb (Ser807/811;clone D20B12, Cell Signalling Technology, #8516S, 1:1000). The secondary antibodies used were highly cross-absorbed goat anti-rabbit or anti-mouse coupled to Alexa Fluor 488 and Alexa Fluor 568 (Thermo Fisher, #A-11029 and #A-11036 respectively) which were both used at 1:1000 dilution. All antibodies were made up in 3% BSA in PBS. For EdU staining, a base click EdU staining kit was used (Sigma, BCK-EDU488), as per manufacturer's instructions.

Time-lapse imaging

For FUCCI time-lapse imaging, cells were plated at low density (approximately 15,000 cells per well) and imaged in 24-well plates in DMEM inside a heated 37°C chamber with 5% CO2. Images were taken every 10 mins with a 10×/0.5 NA air objective using a Zeiss Axio Observer 7 with a CMOS ORCA flash 4.0 camera at 4 × 4 binning. For bright-field imaging, cells were imaged in a 24-well plate in DMEM in a heated chamber (37°C and 5% CO2). Images were taken every 10 mins with a 10×/0.5 NA air objective using a Hamamatsu ORCA-ER camera at 2 × 2 binning on a Zeiss Axiovert 200 M, controlled by Micro-manager software (open source; https://micro-manager.org/) or with a 20×/0.4 NA air objective using a Zeiss Axio Observer 7 (details above). Holographic imaging movies were capture using a Holomonitor M4 microscope to quantify single-cell mitotic volumes, which were calculated using the Holomonitor App Suite version 3.4.0.158. All holomonitor analysis was carried out with a Holomonitor M4. A total of 15,000 cells were plated into either a Sarstedt multiwell, or an Ibidi μ-plate glass-bottomed 24 well plate. After 24hrs cells were treated and imaging began immediately. Images were scheduled every 20 minutes for a total of 96 hours.

Image analysis, quantification, and statistics

For single cell volume traces, 5 cells were randomly selected in the first frame then followed by eye with volume measurements calculated every 2 hours for the duration of the first full cell cycle (mitosis to mitosis) or until the 48hr mark. For population analysis of mitotic volumes, 50 mitotic cells were randomly selected in the first 12 hours following palbociclib treatment. The volume of these mitotic cells were calculated and the resulting daughter cells were followed by eye until they entered mitosis, or the movie ended. The volume of the cell in this second mitosis was calculated and this along with the time between the first and second mitosis was used to determine growth rate. Growth rates were assumed to be linear and were calculated as $\frac{V2-\left(\frac{V1}{2}\right)}{CL}$, where V1 is the cell volume in the first mitosis, V2 is the volume in the second mitosis, and CL is the time between the two (cycle length).

The single-cell FUCCI profiles were generated manually by analysing RPE1-FUCCI movies. A total of 50 red cells were randomly selected and marked at the beginning of the movie. The time points in which the FUCCI cells change colour was recorded to determine the time spent in each phase of the first cell cycle following release from CDK4/6 inhibition. RPE-FUCCI cells were always imaged with the same illumination settings and all images were placed on the same scale prior to analysis to ensure that the red/yellow/green cut-offs were reproducibly calculated between experiments. Mitotic entry was timed based on the visualization of typical mitotic cell rounding and loss of nuclear mAG-geminin signal. For mitotic entry quantifications in brightfield movies, 50 cells were selected at random at the beginning of the time lapse and the time point that each of these cells entered mitosis was determined. Mitotic entry was timed based on nuclear envelop breakdown and cell rounding. For the cumulative G1 exit movies RPE-FUCCI cells

were treated with the indicated range of doses of palbociclib and imaging began immediately, with images being collected every 10 minutes for a total of 48hrs. For analysis 50 G1 (red) cells were selected at random in the first frame of the movie, and these cells were then tracked by eye and the point at which the nucleus changed colour to yellow was taken as the time point of G1 exit.

γH2AX foci were counted by eye in the first 50 cells (per condition) selected using the DAPI channel. For scoring of nuclear abnormalities, the first 100 cells within the image were counted and scored based on their nuclear morphology. Both p21 and EdU intensities were calculated by first using the DAPI channel to generate an ROI overlay in ImageJ. This overlay was then applied to the EdU or p21 channels and used to measure the mean grey value of each individual ROI. An area outside any ROI was then designated as background and its mean grey value in either channel was also calculated. This background value was then subtracted from all ROI values from the corresponding channel.

Statistical significance was determined by Fisher's exact test, unpaired t tests, or Mann-Whitney tests, as indicated in legends. The graphs in Figures 4, S3, and S4A are plotted as violin plots using PlotsOfData[74]; https://huygens.science.uva.nl/PlotsOfData. This allows the spread of data to be accurately visualized along with the 95% confidence intervals (thick vertical bars) calculated around the median (thin horizontal lines). Statistical comparison can then be made by eye between any treatment and time points, because when the vertical bar of one condition does not overlap with one in another condition, the difference between the medians is statistically significant ($P < 0.05$).

Western blotting

Total protein lysates for immunoblot were prepared by scraping cells into 4X protein loading buffer (250mM Tris, 10% SDS, 40% Glycerol, 0.1% Bromophenol Blue) and then sonicating with a Cole-Parmer ultrasonic processor (20% Amp, 15 sec pulse). Samples were briefly boiled and centrifuged followed by a DC assay to determine protein concentration, after which 2-mercaptoethanol was added at a final concentration of 10%. Equal concentrations of protein were loaded and then separated on SDS—PAGE gels and transferred to 0.45μm nitrocellulose membranes (Amersham Protran Premium). After transfer, blots were blocked in 5% milk in TBS with 0.1% Tween 20 (TBS-T) and incubated overnight at 4°C in primary antibody in TBS-T. Membranes were then washed three times in TBS-T, incubated in IRDye secondary antibody for 2h, and washed 3 further times prior to visualisation on a LI-COR Odyssey CLx system. The primary antibodies used were rabbit pS6 (Phospho-S6 Ribosomal Protein; Ser235/236, Cell Signalling, 4858, 1/1000), rabbit actin (Sigma, A2066, 1/5000) rabbit pAKT (Ser473, Cell Signalling, 4060S, 1/1000), rabbit AKT (Cell Signalling, 9272, 1/1000), rabbit ERK1/2 (Upstate, 06-182, 1/1000), mouse p-p44/42 (pERK1/2 Thr202/Try204, Cell Signalling, 9106S), 1/1000), rabbit p21 Waf1/Cip1 (clone 12D1, Cell Signaling Technology, #2947, 1:1000), mouse p53 (Clone DO-1, Santa Cruz, sc-126, 1/1,000). Secondary antibodies used were: IRDye 800CW Goat anti-Mouse IgG (LI-COR, 926-32210), IRDye 800CW Donkey anti-Rabbit IgG (LI-COR, 926-32213)., IRDye 680RD Goat anti-rabbit IgG (LI-COR, 925-68071), IRDye 680RD Goat anti-mouse IgG (LI-COR, 925-68070). All LI-COR secondary antibodies were used at a 1/15,000 dilution.

Colony-forming assays

For the colony-forming assays, cells were treated with palbociclib at 60,000 cells per 10 cm dish for different lengths of time (1–7 days) prior to drug washout (6 × 1 h washes). Following washing and trypsinization, RPE1 and MCF10As were plated in triplicate at 250 cells into 10 cm dishes and left to grow for 10 days, whereas MCF7 and T47Ds were plated at 500 cells in triplicate in 6-well plates and allowed to grow for 14–21 days. ARPE19 cells were plated at 250 cells in triplicate in 6-well plates and allowed to grow for 10 days. At the end of the assay, cells were washed twice in PBS and then fixed at 100% ethanol for 5 min. Developing solution (1:1 ratio of 2% Borax:2% Toluene-D in water) was added to the fixed cells for 5 min and the plates were then rinsed thoroughly with water and left to dry overnight. The plates were then scanned, and the number of colonies were quantified using ImageJ. This was performed by cropping to an individual plate and converting to a binary image. The fill holes, watershed and analyse particles functions were then used to count colonies.

Weekly fold increase in cell count

A total of 60,000 cells from each MCF10A line were plated into 10 cm dishes and treated with palbociclib (1 μM) or DMSO (control). After 7 days of treatment, cells were trypsinized, and counted using an NC-3000 Nucleocounter to calculate the 7-day fold increase in cell number. From the cell suspension, 60,000 cells were returned to palbociclib treatment, and this process was repeated two more times for a total of 3 weeks. At each time point, excess cells were transferred to coverslips and taken for immunofluorescence with γH2AX antibodies to assess DNA damage.

Proteomics

Cells were scraped in 2% SDS lysis buffer containing phosphatase inhibitors (PhosStop, Roche) and protease inhibitors (Complete EDTA-free, Roche). Extracts were heated to 95 °C, cooled to room temperature, and treated with benzonase (Millipore, 70664) for 30 min at 37 °C. The benzonase treatment was repeated until the extract was free flowing. The protein concentration was determined and 50 μg protein aliquots were precipitated using acetone-ethanol. Precipitated protein was then digested with trypsin (1:100), once for 16 hours before another aliquot of trypsin is added (1:100) and incubated for an additional 4 hours. Peptides were then desalted using SepPak cartridges (Waters).

Peptides were analyzed by LC-MS/MS using a data-independent acquisition (DIA) approach implemented on a RSLCnano HPLC (Dionex) coupled to an Orbitrap Exploris 480 mass spectrometer (Thermo) using DIA windows reported previously.[80] Peptides were separated on a 50-cm (2-μm particle size) EASY-Spray column (Thermo Fisher Scientific), which was assembled on an EASY-Spray source (Thermo Fisher Scientific) and operated constantly at 50 °C. Mobile phase A consisted of 0.1% formic acid in LC–MS-grade water and mobile phase B consisted of 80% acetonitrile and 0.1% formic acid. Peptides were loaded on to the column at a flow rate of 0.3 μl min^{-1} and eluted at a flow rate of 0.25 μl min^{-1} according to the following gradient: 2–40% mobile phase B in 120 min and then to 95% in 11 min. Mobile phase B was retained at 95% for 5 min and returned back to 2% a minute after until the end of the run (160 min in total).

The spray voltage was set at 2.2 kV and the ion capillary temperature at 280 °C. Survey scans were performed at 15,000 resolution, with a scan range of 350–1,500 *m/z*, maximum injection time 50 ms and AGC target 4.5×10^5. MS/MS DIA was performed in the Orbitrap at 30,000 resolution with a scan range of 200–2,000 *m/z*. The mass range was set to 'normal', the maximum injection time to 54 ms and the AGC target to 2.0×10^5. An inclusion mass list with the corresponding isolation windows was used as previously reported. Data for both survey and MS/MS scans were acquired in profile mode. A blank sample (0.1% TFA, 80% MeCN, 1:1 v:v) was run between each sample to avoid carryover.

Proteomics Data Analysis

Raw files were analyzed using Spectronaut 16.2.220903.53000 (Biognosys) by directDIA using a 0.01 cutoff value for Precursor Qvalue, Precusor Posterior Error Probability (PEP) and Protein Qvalue. Carbamidomethyl was set as a fixed modification and Acetyl (N-term), Deamidation (NQ), Dioxidation (MW), Gln->pyroGlu and Oxidation (M) were set as variable modifications. No imputation was performed and the LFQ method was set to "QUANT 2.0 (SN Standard)". The data were searched against the UniProt human reference proteome (accessed May 11th, 2021).

Protein-level intensities were then normalized two ways: 1) to protein copies using the proteomic ruler[81] and 2) to concentrations by dividing intensities for individual proteins against the total intensity and multiplying by 1e6 (parts per million, ppm).[82]